Opposing Changes in Mean Climate Diminish the Sensitivity

of ENSO Simulations to Increasing Greenhouse Gases

Pedro N. DiNezio

Cooperative Institute for Marine and Atmospheric Studies, University of Miami, Miami, Florida

Rosenstiel School of Marine and Atmospheric Science, University of Miami, Miami, Florida

NOAA/Atlantic Oceanographic and Meteorological Laboratory, Miami, Florida

Ben P. Kirtman

Rosenstiel School of Marine and Atmospheric Science, University of Miami, Miami, Florida

Amy C. Clement

Rosenstiel School of Marine and Atmospheric Science, University of Miami, Miami, Florida

Sang-Ki Lee

Cooperative Institute for Marine and Atmospheric Studies, University of Miami, Miami, Florida

NOAA/Atlantic Oceanographic and Meteorological Laboratory, Miami, Florida

Gabriel A. Vecchi

NOAA/Geophysical Fluid Dynamics Laboratory, Princeton, New Jersey

Andrew Wittenberg

NOAA/Geophysical Fluid Dynamics Laboratory, Princeton, New Jersey

To be submitted to J. Climate

_____

Corresponding author address: Pedro N. DiNezio, Cooperative Institute for Marine and Atmospheric Studies, Rosenstiel School of Marine and Atmospheric Science, University of Miami, 4600 Rickenbacker Causeway, Miami, FL 33149.

E-mail: pdinezio@rsmas.miami.edu

30

Abstract

32   Here, we perform a multi-model heat budget analysis of CO2-doubling (2xCO2)
33 climate change experiments coordinated by the Coupled Model Intercomparison Project
34 phase 3 (CMIP3) to elucidate if and how the changes in the mean climate affect ENSO.
35 We find that the weakening of the Walker circulation and the increased thermal
36 stratification, both robust features of the mean climate response to 2xCO2, play opposing
37 roles in ENSO – mean climate interactions. The opposing roles in these interactions
38 explain the lack of model agreement in whether ENSO is going to weaken or strengthen
39 in response to increasing greenhouse gases. We perform a multi-model heat budget
40 analysis of CO2-doubling climate change experiments coordinated by the Coupled Model
41 Intercomparison Project phase 3 (CMIP3) in order to elucidate the details of ENSO –
42 mean climate interactions. In specific, the weakening of the mean equatorial upwelling in
43 response to weaker Walker circulation drives a reduction in thermocline-driven ocean
44 heat convergence (i.e., thermocline feedback), and thus reduces the ENSO amplitude. On
45 the other hand, a stronger mean zonal subsurface temperature gradient, associated with
46 the increased thermal stratification, drives an increase in zonal current-induced ocean
47 heat convergence (i.e., zonal advection feedback), and thus increases the ENSO
48 amplitude. Therefore, whether ENSO amplitude increases or decreases in a particular
49 model depends critically on the balance between the thermocline feedback and advection
50 feedback in that model, explaining the lack of model agreement.

1. Introduction

Increasing greenhouse gas (GHG) experiments coordinated by the Coupled Model Intercomparison Project phase 3 (CMIP3) do not agree whether El Nino/Southern Oscillation (ENSO) is going to strengthen or weaken. Whether ENSO has changed due to recent observed warming is also controversial according the observational record (e.g. Trenberth and Hoar 1997; Harrison and Larkin 1997; Rajagopalan et al. 1997). For these reasons, the Intergovernmental Panel on Climate Change (IPCC) Fourth Assessment Report (AR4) concluded that there is no consistent indication of discernible changes ENSO amplitude in response to increasing GHGs (Meehl et al. 2007). Given that ENSO is the dominant mode of tropical variability, the lack of agreement among models is an important source of uncertainty for projecting future regional climate change throughout the Pacific basin (IPCC AR4).

In contrast, the CMIP3 models largely agree in the response of the mean ocean climate, i.e. the background ocean conditions over which ENSO variability occurs. This is, when forced with increasing GHGs, the great majority of models simulate a shoaled, less tilted, and sharper thermocline; weaker zonal currents; and weaker upwelling (Vecchi and Soden 2007; DiNezio et al. 2009). These robust ocean responses are driven by a weakening of the Walker circulation, for which there is observational evidence (Vecchi et al. 2006). ENSO theory indicates that any of these changes in the mean climate can lead to changes in ENSO amplitude, yet their direct influence on ENSO is not evident (Vecchi and Wittenberg 2010; Collins et al. 2010).

72   Theoretical, observational, and modeling studies have linked changes in the

73   thermocline with changes in ENSO amplitude. The instability analysis of Fedorov and

74   Philander (2001) showed that a sharper thermocline leads to weaker ENSO amplitude in

75   a simple coupled ocean–atmosphere model. Conversely, their model simulates a stronger

76   ENSO in response to a shallower thermocline. Observations, in contrast, suggest that the

77   strong ENSO events of the 1980s and 1990s could be a result of a deepening of the

78   thermocline after the 1976 climate shift (Guilderson and Schrag 1998) or a sharper

79   thermocline due to GHG related warming (Zhang et al. 2008). However, the

80   observational evidence is not conclusive because: 1) there is evidence of strong ENSO

81   activity before the 20th Century (e.g. Grove 1988) and 2) ENSO has been relatively quiet

82   during the first decade of the 21th Century despite continued warming. General

83   circulation models (GCMs) exhibit a robust relationship between increased ENSO

84   amplitude and reduced vertical diffusivity (i.e. a sharper thermocline) in the equatorial

85   thermocline (Meehl et al 2001). This relationship explains why the previous generation

86   ocean models, which had very diffuse thermoclines, simulated much weaker ENSO

87   variability than observed. Conversely, a sharper thermocline has been invoked to explain

88   the increase ENSO amplitude in some increasing GHG experiments (e.g. Timmermann et

89   al. 1999; Park et al. 2009).

90   All models participating in CMIP3 simulate a sharper thermocline in response to

91   increasing GHGs, yet not all of them simulate a stronger ENSO. Other physical

92   processes, such as the shoaling of the thermocline, weaker upwelling, or warmer mean

93   SST could also have an amplifying or damping effect on ENSO. Thus, it is reasonable to

94   hypothesize that depending on the balance of these changes; ENSO could strengthen or

95   weaken (Vecchi and Wittenberg 2010; Collins et al. 2010). A few studies, however, have

96   actually attempted to isolate and quantify the contribution from each feedback (van

97   Oldenborgh et al. 2005; Philip and van Oldenborgh 2006; Kim and Jin 2010a, 2010b).

98   Philip and van Oldenborgh (2006) used a simplified SST equation to show that the

99   shoaling of the thermocline enhances ENSO variability, but the warmer mean SST results

100   in stronger atmospheric damping. Kim and Jin (2010b), used the Bjerknes (BJ) index to

101   show how, depending on the balance among the different ENSO feedbacks, the changes

102   in mean climate are directly related to whether ENSO strengthens or weakens in response

103   to increasing GHGs. However, because the BJ index is computed for the Nino-3 region,

104   the results do not indicate the spatial patterns involved in the ENSO-mean climate

105   interaction.

106   In this paper we also quantify the contribution from the robust changes in the

107   mean climate on ENSO as simulated by CMIP3 models. However, we perform a heat

108   budget analysis of ENSO variability directly from the output of an ensemble of 10

109   coupled GCMs. The heat budget is computed as a balance between the heat storage rate,

110   the advective heat flux convergence, and the net atmospheric heat flux. In contrast with

111   the studies discussed above, computing the advective terms on every grid point allows us

112   to explore the spatial pattern of the interaction between ENSO anomalies and changes in

113   mean ocean climate. The methodology also allows us to closely balances the heat budget

114   in all models, increasing our confidence in the attribution of the ENSO changes. This is

115   key advantage over previous methodologies, which do not necessarily satisfy the

116   requirement of a balanced heat budget. Finally, we use the changes in the heat budget to

117   show how robust changes in the mean ocean climate drive opposing effects resulting in

118   the wide range of ENSO responses exhibited by the CMIP3 models.

2. Global Warming Experiments

In this study we analyze both changes in ENSO variability and in the mean climate of the equatorial Pacific as simulated in climate model experiments coordinated by CMIP3. A pre-industrial control experiment is used as a base-line climate. An idealized experiment in which atmospheric CO2 is doubled (2xCO2) with respect to pre-industrial levels is used to compute the changes in ENSO and the mean climate. For all models, the pre-industrial climate experiment was forced with 280 ppm of CO2 and 760 ppb of CH4. This is the "picntrl" experiment in the CMIP3 database. See Table 1 for a list of models used in this study.

The idealized 2xCO2 experiment starts from the picntrl experiment, increasing CO2 concentrations at a rate of 1% yr^{-1} from 280 ppm until doubling at 560 ppm on year 71. Then the experiment is run 150 additional years with constant 2xCO2 forcing. This is the "1pctto2x" experiment in the CMIP3 database. All ENSO statistics and heat budgets for the 2xCO2 climate are computed using model output from the last 150 years of the 1pctto2x experiment. The models still exhibit warming trends of less than 0.4 K $year^{-1}$ during the last 150 years of this experiment. However, these trends are small compared with the warming of about 2K during the first 71 years when the GHG forcing is largest. The 2xCO2 changes in the mean climate are computed by differencing the annual-mean climatology from the 2xCO2 (1pctto2x) experiment minus the annual-mean climatology from the pre-industrial (picntrl) experiment. The 2xCO2 changes in ENSO are computed by differencing the ENSO statistics during the 150 years of quasi-equilibrated 2xCO2 climate (1pctto2x) minus the ENSO statistics during the 500 years pre-industrial climate.

141   Section 3 analyzes the ocean processes involved in the growth of ENSO events in

142   the *unperturbed* pre-industrial climate. We first compute ENSO anomalies with respect to

143   the climatological seasonal cycle. Then, we regress these anomalies on the tendency of

144   the Nino-3 index ($\partial N3/\partial t$ index) in order to estimate the magnitude and spatial pattern of

145   the physical processes involved in the development phase of ENSO events. More details

146   on this can be found in the appendix. Section 4 presents the attribution of the ENSO

147   response to the increases in GHGs.

Robustness

149   Throughout this study we focus on those aspects of the ENSO mechanisms and

150   their response to 2xC02 that appear in the multi-model mean. To provide an indication of

151   how robust these signals are across the different models, we also indicate where models

152   agree with the sign of the multi-model mean anomaly or change (e.g., Figure 2, non

153   stippled areas). This estimate of robustness does not provide information about how close

154   the model anomalies/changes are to the multi-model mean, and thus is not useful to

155   detect outliers. However, it remains useful in our study, because much of the debate on

156   the sensitivity of ENSO to increasing GHGs has been on the sign of the amplitude change

157   (i.e. weaker or stronger). In addition, we analyzed the response by each individual model

158   to avoid making erroneous conclusions from the multi-model mean.

3. Robust ENSO Mechanisms

a) Recharge mode

All models simulate thermocline anomalies with spatial pattern and time evolution indicating their fundamental role in the development, transition, and decay of ENSO events. In all models, thermocline depth anomalies (Z'_{TC}) and sea surface temperature anomalies (*SSTA*) are in quadrature throughout the ENSO cycle (Figure 1, red and blue lineas respectively). The multi-model composite shows that the thermocline deepens (red line) about 10 months before the maximum warming of the cold tongue (blue line). The thermocline shoals about a year later, driving the transition into the cold phase of the ENSO cycle.

The multi-model composite heat budget, also shows that the anomalous heat storage rate ($Q'_t = \rho_0 c_p H \partial T' / \partial t$) results entirely from the anomalous ocean heat flux convergence (Q'_{ocn}), which is in phase with Z'_{TC} (Figure 1). Thus, ocean dynamics, and in particular the thermocline, play a fundamental role in the generation of ENSO events in all models. We take advantage of this close relationship and, throughout our analysis, regress anomalies on the tendency of the Nino-3 index ($\partial N3 / \partial t$ index) in order to capture the magnitude and spatial pattern of the different physical processes driving Q'_{ocn}. More details on these regressions can be found in the appendix.

The multi-model changes in thermocline depth revealed by the regressions on the $\partial N3 / \partial t$ index exhibit a zonal mean deepening over the equatorial wave-guide (Figure 2a). The models also simulate increased sea level consistent with a deeper thermocline (Figure 2b). Thus, both the phasing between Z'_{TC} , Q'_{ocn}, and *SSTA* (Figure 1, red, black,

181   and grey lines respectively) and the spatial pattern of Z'_{TC} prior to the development of

182   ENSO events are consistent with the recharge oscillator (Jin 1997) or with the delayed

183   oscillator (Schopf and Suarez 1987; Battisti 1988; Suarez and Schopf 1988; Battisti and

184   Hirst 1989).

185   The subsurface temperature anomalies also show the signature of a deeper

186   thermocline as warm ENSO events develop (Figure 3). The multi-model regressions of

187   equatorial temperature exhibit an anomalous subsurface warming at the depth of the

188   thermocline in the central and western Pacific indicative of a deepening of the equatorial

189   thermocline (Figure 3a). These anomalies are accompanied by decreased (increased)

190   vertical stratification above (below) the time-mean thermocline (Figure 3b, the time-

191   mean thermocline depth is shown by the dash-dotted line). The anomalously weak

192   stratification in the upper ocean should reduce the ocean dynamical cooling associated

193   with climatological upwelling (i.e., $-\overline{w}\,\partial T'/\partial z > 0$ in the RHS of equation A1, primed

194   variables indicate ENSO anomalies and bar variables are the mean seasonal climate). In

195   the next subsection we show that this is the main mechanism contributing to the

196   anomalous convergence of heat by ocean processes during the development of warm

197   ENSO events.

198   The multi-model regressions of the anomalous surface stratification, zonal

199   currents, and upwelling show where, along the equatorial Pacific, they contribute to the

200   development of ENSO events. The deepening of the thermocline drives anomalously

201   weak stratification $\partial T'/\partial z$, in the upper 100 m of the ocean over the central Pacific

202   (Figure 4a, colors) where the mean equatorial upwelling is also strongest (Figure 4a,

203   contours). This suggests that during the development phase of ENSO events the

10

204   anomalous ocean heat flux convergence (hereafter ENSO heat flux convergence) results

205   from the vertical advection of thermocline temperature gradient anomalies by

206   climatological upwelling (i.e. $-\overline{w}\,\partial T'/\partial z > 0$). The zonal currents during the

207   development phase (estimated from the regressions) exhibit eastward anomalies located

208   in the eastern Pacific (Figure 4b, colors). In the presence of the climatological zonal SST

209   gradient (Figure 4b, contours), these anomalies also contribute to the ENSO heat flux

210   convergence (i.e. $-u'\,\partial \overline{T}/\partial x > 0$).

211   Wind anomalies are negligible during the recharge or development phase, thus the

212   current anomalies u', estimated with the regressions cannot be driven by local winds,

213   which only weaken when the ENSO *SSTA* is developed. However, the regressions are

214   consistent with the dynamics of the recharge mode, which has associated zonal current

215   anomalies (Kirtman 1997; Clarke 2010), since it is a packet of Kelvin waves reflected

216   from the western boundary as a result of the wind stress curl (WSC)-forced Rossby

217   waves. Geostrophy and the meridional gradients in the thermocline anomalies can also

218   lead to zonal current anomalies, however not on the equator (Jin et al 2006).

219   Vertical velocity during developing ENSO events w', exhibits anomalous

220   downwelling located in the eastern Pacific (Figure 4c, colors). This downwelling is not a

221   response to local winds, since the trade winds do not weaken until the ENSO SSTAs

222   develop, but is consistent with the convergence of the anomalous zonal currents in

223   eastern boundary. The meridional currents at this stage of the ENSO cycle are only

224   significant on the coast (not shown), suggesting coastally trapped Kelvin waves.

225   However these anomalous currents diverge on the equator, thus driving upwelling. Thus,

226   the anomalous downwelling suggested by w' (Figure 4c) can only be explained by the

227   convergence of *u'* (Figure 4b). In the presence of the climatological stratification (Figure

228   4c, contours), the anomalous downwelling must also contribute to the ENSO heat flux

229   convergence.

230   *b)   Linear ENSO Heat Budget*

231   The anomalous heat flux convergence associated with anomalous thermocline

232   Q'_{tc}, zonal currents Q'_u, and upwelling Q'_w, are estimated as the advection of temperature

233   anomalies (primed quantities) by climatological fields (bar quantities) as:

234    $$Q'_{tc} = -\rho_0 c_p \int_{-H}^{0} \left(\overline{w} \frac{\partial T'}{\partial z} \right) dz \qquad (1a),$$

235    $$Q'_u = -\rho_0 c_p \int_{-H}^{0} \left(u' \frac{\partial \overline{T}}{\partial x} \right) dz \qquad (1b),$$

236    $$Q'_w = -\rho_0 c_p \int_{-H}^{0} \left(w' \frac{\partial \overline{T}}{\partial z} \right) dz \qquad (1c).$$

237   We use resolved monthly-mean ocean fields to compute these terms of the linear heat

238   budget because these are the highest resolution ocean data available in the CMIP3

239   database. The primed quantities are anomalies with respect to the climatological annual

240   cycle.

241   The multi-model regressions of these fields on the $\partial N3/\partial t$ index indicate that

242   during the development of ENSO events, the anomalous ocean heat flux convergence due

243   to thermocline anomalies Q'_{tc}, is concentrated in a narrow band in the central equatorial

244   Pacific (Figure 5a). Note that the largest Q'_{tc} coincides where the climatological

245   upwelling $\overline{w}$, is strongest (Figure 4a, contours). The anomalous heat flux convergence

12

246   due to zonal currents Q'_u, is strongest in the eastern Pacific (Figure 5b) coincident with

247   the location of the anomalous zonal currents (Figure 4b, colors). The heating due to

248   upwelling Q'_w, is strongest in the eastern Pacific close to the coast of South America

249   (Figure 5c) coincident with the location of the anomalous downwelling (Figure 4c,

250   colors). Note that we do to include the effect of meridional currents in the heat flux

251   convergence, $-\left(v'\,\partial\overline{T}/\partial y + \overline{v}\,\partial T'/\partial y\right)$, because these terms tend to cancel each other on

252   ENSO timescales. This point will become clearer in the following discussion on

253   intermodel differences in Q'_{tc}, Q'_u, and Q'_w (Figure 7). Air-sea heat fluxes could also

254   play a role in the development of SSTAs, however the regressions indicate that they are

255   negligible on the equatorial band (Figure 5d). This is consistent with the composite heat

256   budget (Figure 1, green line), which shows that the air-sea heat flux damps the SSTA

257   throughout the entire ENSO cycle since it is anti-correlated with the *SSTA*.

258   The vertical distribution of the temperature tendencies associated with the

259   thermocline zonal current, and downwelling anomalies shows more details on the

260   mechanisms discussed above (Figure 6). Note that the temperature tendencies shown in

261   Figure 6 are not dependent on the depth of integration *H*. The temperature tendencies due

262   to the changes in thermocline depth occur in the upper 100 m (Figure 6a) and are largest

263   in the central equatorial Pacific, where the climatological equatorial upwelling is

264   strongest.

265   The temperature tendencies due to the anomalous zonal currents are large below

266   the surface (Figure 6b) where the largest climatological zonal temperature gradients are

267   located. The zonal current anomalies are strongest in the surface between 150ºW and

268   90ºW (Figure 4b) where, unlike observations, the zonal SST gradient is weak. This

269   occurs because the equatorial cold tongue extends too far to the west in coupled climate

270   models. However, Q'_u is large in the subsurface due to the zonal temperature gradient

271   associated with the east-west tilt of the thermocline. This is a clear example of how biases

272   in the simulation of the mean climate can result in an unrealistic balance among ENSO

273   mechanisms. The temperature tendencies due to the anomalous upwelling are large close

274   to the eastern boundary (Figure 6c) where the downwelling anomalies and the

275   climatological stratification are large (Figure 4c).

276   In all the models Q'_{tc} is strongest over a narrow area in the equatorial waveguide

277   coinciding approximately with the Nino-3.4 region. This region is where coupling

278   between SST, wind, and thermocline anomalies is strongest due to the presence of east-

279   west gradients in the climatological SST and thermocline depth (Suarez and Schopf

280   1988). In this study the Nino-3.4 region is defined as the area 180º-110ºW 2.5ºS-2.5ºN,

281   which is shifted more westward and meridionally narrower than the observational

282   definition, in order to account for SST biases in the models. The total heat convergence

283   due to monthly-mean currents Q'_{adv}, averaged over this Nino-3.4 region is closely related

284   the sum of Q'_{tc}, Q'_u, and Q'_w (Figure 7a). Note that we compute Q'_{adv} (y-axis) using all

285   three components of the monthly-mean velocity field (see equation A.2), including

286   meridional currents. In contrast the linear Q'_{adv} (x-axis) is the sum of Q'_{tc}, Q'_u, and Q'_w

287   as defined in (1). Moreover, Q'_{adv} does not necessarily need to balance the heat budget

288   because it does not include the effect of mixing, parametrized eddies, and sub-monthly

289   resolved currents. In contrast, Q'_{ocn} includes all ocean processes because it is computed

290   as a residual from the heat storage rate and the atmospheric heat fluxes. The appendix

14

291 shows how Q'_{adv} nearly balances the heat budget on ENSO timescales, thus can be used

292 to study the interaction of ENSO and the changes in mean climate due to 2xCO2.

293   The models also exhibit differences in how the advective terms of the linear heat

294 budget (1) contribute to the development of ENSO events. The advective heat flux

295 convergence Q'_{adv}, is dominated by Q'_{tc}, and model values ranging from 5 to 40 Wm^{-2}

296 (Figure 7b). Anomalous zonal currents also contribute to Q'_{adv} (Figure 7c) with values of

297 Q'_{u} ranging from 5 to 20 Wm^{-2}. In contrast, Q'_{w} is negligible over Nino-3.4 in all models

298 (not shown), with the exception of CCCma-CGCM3.1 in which Q'_{adv} dominates with

299 values of 8 Wm^{-2}. MIROC3.2, CCCma-CGCM3.1, and INM CM3 simulate much weaker

300 Q'_{adv} due to a much weaker Q'_{tc} (Figure 7b). These models simulate much smaller ENSO

301 thermocline depth anomalies that the models with stronger ENSO events; yet, their

302 climatological thermocline is as sharp. In contrast, the models with weak ENSO (in the

303 control climate) exhibit a localized steep east–west gradients or "thermocline jumps",

304 which could suppress the westward propagation of thermocline anomalies and hence

305 suppress ENSO variability (Spencer et al. 2007).

4. ENSO Response to Global Warming

306

307   The coupled models analyzed here do not agree in the sign of the changes in

308 ENSO amplitude in response to global warming as reported by previous studies (van

309 Oldenborgh et al. 2005; Philip and van Oldenborgh 2006; Guilyardi 2006; Merryfield

310 2006). The inter-model differences in the changes in ENSO amplitude are directly linked

311 to the inter-model differences in the 2xCO2 change in ENSO ocean heat convergence,

312 $\Delta Q'_{ocn}$ (Figure 8). Here we compute the change in ENSO amplitude as the difference in

313   standard deviation of the (dimensional) N3 index between the 2xCO2 and pre-industrial

314   climates. The models with stronger ENSO amplitudes in the 2xCO2 climate (y-axis)

315   exhibit increased Q'_{ocn}, (x-axis), and vice-versa. For instance, GFDL-CM2.1 and

316   simulates an increase in ENSO amplitude of about 0.2 K along with an increase in Q'_{ocn}

317   of about 7 Wm^{-2} and FGOALS-g1.0 simulates a reduction in ENSO amplitude of about

318   0.5 K commensurate with a reduction in Q'_{ocn} of about 7 Wm^{-2}.

319   The close relationship between the 2xCO2 changes in ENSO amplitude and in

320   ENSO heat flux convergence $\Delta Q'_{ocn}$, is not unexpected because, as discussed in Section

321   3, SST anomalies not only result from, but also drive the changes in Q'_{ocn} via the

322   Bjerknes feedback. Thus a cause-and-effect link cannot be immediately established.

323   Moreover, because the 2xCO2 climate is computed from just 150 years, the 2xCO2

324   changes could arise from unforced centennial changes in ENSO amplitude. A recent

325   modeling study using GFDL-CM2.1 has suggested that multi-decadal and centennial

326   changes in ENSO amplitude are possible, even in the absence of external forcing,

327   (Wittenberg 2009). Thus, given the shortness of the 1% to CO2-doubling (1pctto2x)

328   experiment, the changes in ENSO amplitude computed from the last 150 years may not

329   isolate the response to 2xCO2 forcing.

330   In order to determine whether the changes in amplitude are due to 2xCO2 forcing

331   we compare them with estimates of centennial changes in ENSO amplitude from the pre-

332   industrial control experiments. The range of possible multi-decadal and centennial

333   unforced changes in ENSO amplitude is computed as the standard deviation between the

334   different ENSO amplitudes during overlapping 100-year periods taken every 50 years

335   from the pre-industrial experiments. These estimates of uncertainty are shown in Figure 8

16

336 as vertical error bars. Most of the models exhibit changes in amplitude that are larger than

337 the range of unforced centennial changes, and therefore are attributable to 2xCO2. The

338 large uncertainty exhibited by GFDL-CM2.1 is consistent with the results of Wittenberg

339 (2009), yet the 2xCO2 change in ENSO amplitude is very likely to be externally forced

340 because it is larger than the unforced 1σ range of ENSO amplitudes.

341   The spatial patterns of the 2xCO2 changes in ENSO heat flux convergence,

342 $\Delta Q'_{ocn}$ also correspond with the spatial pattern of the 2xCO2 changes in ENSO

343 amplitude, $\Delta SSTA$ (Figure 9). The models that simulate stronger ENSO amplitude in the

344 2xCO2 climate (GFDL-CM2.1, MRI-CGM2.3.2a) show a pattern of positive $\Delta SSTA$

345 (Figure 9a) and positive $\Delta Q'_{ocn}$ (Figure 9c) concentrated in the central Pacific. The

346 models that simulate weaker ENSO in the 2xCO2 climate (CCSM3.0, FGOALS-g1.0,

347 IPSL-CM4), show a pattern of negative $\Delta SSTA$ (Figure 9b) and negative $\Delta Q'_{ocn}$ (Figure

348 9d) concentrated in the central Pacific. Note that the models with stronger ENSO in the

349 mean climate have $\Delta SSTA$ and $\Delta Q'_{ocn}$ displaced.

350   Changes in ENSO amplitude and ocean heat flux convergence can result from

351 changes in the branch of the Bjerknes feedback-loop involving SST and wind changes,

352 even in the absence of changes in background ocean conditions. This involves the

353 response of the equatorial trade winds to a given SST anomaly, and depends mostly on

354 how the Walker circulation responds to latent heat release associated with convective

355 precipitation. The sensitivity of these processes can certainly change as the atmosphere

356 warms up in response to the 2xCO2 forcing. We quantify the strength of the wind-SST

357 coupling by defining a coupling coefficient as the regression coefficient between the

358 monthly anomalies of zonal surface wind stress in the Nino-4 region (140E°-160ºW 5ºS-

17

359   5ºN) and SST in the Nino-3.4 region (Guilyardi 2006). A large coupling coefficient

360   indicates a stronger response of the trade winds for the same magnitude of anomalous

361   warming. The inter-model differences in coupling strength do not explain the inter-model

362   differences in ENSO amplitude in the control climate (inter-model r = -0.08, not shown).

363   Some of the models exhibit large changes in coupling coefficient in the 2xCO2 climate,

364   however, these changes are not related to the changes in the Q'_{tc} (inter-model r = -0.16;

365   Figure 10) nor ENSO amplitude. For instance IPSL-CM4 and FGOALS-g1.0 exhibit

366   increases in coupling of 25% and 9% respectively, but they fail to translate into increased

367   ENSO amplitude.

368   In contrast, the changes in Q'_{ocn} are related to the changes in Q'_{tc} and Q'_u. In

369   general, the models with increased ENSO amplitudes also exhibit an increase of all three

370   terms of the linear heat budget. Note that the inter-model $\Delta Q'_{ocn}$, are well captured by the

371   inter-model changes in advective heat flux convergence, $\Delta Q'_{adv}$ (Figure 11a). This allows

372   us to use the linear decomposition of the heat budget. The models show a close

373   relationship with $\Delta Q'_{tc}$ (Figure 11b) and $\Delta Q'_u$ (Figure 11d) averaged over the Nino-3.4

374   region (inter-model r = 0.82 and r = 0.71 respectively). We compare the changes in

375   heating averaged over Nino-3.4 region, because this is where the resulting SST changes

376   are most effective at influencing the atmospheric circulation, closing the ENSO feedback

377   loop. Not all models exhibit downwelling anomalies in the central Pacific (not shown),

378   this is why not all the models show a close relationship with upwelling $\Delta Q'_w$, (Figure

379   11c). Particularly, the models with reduced ENSO amplitude in the 2xCO2 climate do not

380   exhibit changes in Q'_w (Figure 11c, models CCSM3.0, FGOALS-g1.0, IPSL-CM4).

381   However, $\Delta Q'_{ocn}$ cannot be used to attribute the 2xCO2 changes in ENSO

382   amplitude without entering into a circular argument because of the Bjerknes feedback.

383   For instance, according to (1a), Q'_{tc} can change through changes in the mean upwelling

384     $\Delta\overline{w}$, or changes in the anomalous stratification $\Delta\left(\partial T'/\partial z\right)$. However, only the former is

385   directly related to the 2xCO2 changes in mean climate, while $\Delta\left(\partial T'/\partial z\right)$ is to the change

386   in ENSO amplitude.

387   The influence of the changes in the mean climate on ENSO becomes clear when

388   the changes in each term of the linear ENSO heat flux convergence (1) are computed:

389
$$\Delta Q'_{tc} = -\rho_0 c_p \int_{-H}^{0}\left(\Delta\overline{w}\frac{\partial T'}{\partial z} + \left(\overline{w}+\Delta\overline{w}\right)\Delta\left(\frac{\partial T'}{\partial z}\right)\right)dz \qquad (2a),$$

390
$$\Delta Q'_{u} = -\rho_0 c_p \int_{-H}^{0}\left(u'\Delta\left(\frac{\partial\overline{T}}{\partial x}\right) + \Delta u'\left(\frac{\partial\overline{T}}{\partial x}+\Delta\left(\frac{\partial\overline{T}}{\partial x}\right)\right)\right)dz \qquad (2b),$$

391
$$\Delta Q'_{w} = -\rho_0 c_p \int_{-H}^{0}\left(w'\Delta\left(\frac{\partial\overline{T}}{\partial z}\right) + \Delta w'\left(\frac{\partial\overline{T}}{\partial z}+\Delta\left(\frac{\partial\overline{T}}{\partial z}\right)\right)\right)dz \qquad (2c).$$

392   Throughout this paper the delta notation Δ, refers to 2xCO2 climate changes and primed

393   quantities are ENSO anomalies, e.g. w' are the upwelling anomalies with respect to the

394   monthly-mean seasonal cycle, which in the equatorial band are dominated by ENSO

395   variability. Thus, the Δ operator applied to a primed quantify indicates a 2xCO2 change

396   in an ENSO anomaly. Conversely, a delta applied to a bar quantity indicates a change in

397   mean climate.

398   Equation (2) shows that the changes in Q'_{ocn} cannot be immediately used to

399   attribute changes in ENSO amplitude because the second term in (2) includes 2xCO2

19

400 changes in ENSO anomalies ($\Delta \partial T'/\partial z$, $\Delta u'$, $\Delta w'$), leading to a circular argument.

401 However, the first term in the integrand of (2) involves the 2xCO2 changes in the mean

402 climate ($\Delta \overline{w}, \Delta \partial \overline{T}/\partial x, \Delta \partial \overline{T}/\partial z$) and the ENSO anomalies in the control climate

403 ($\partial T'/\partial z$, u', w'). Thus, these terms can be used to quantify the effect of the changes in

404 mean climate on ENSO heat flux convergence as:

$$\Delta Q'_{mean} = -\rho_0 c_p \int_{-H}^{0} \left(\Delta \overline{w} \frac{\partial T'}{\partial z} + u' \Delta \left(\frac{\partial \overline{T}}{\partial x} \right) + w' \Delta \left(\frac{\partial \overline{T}}{\partial z} \right) \right) dz \ . \qquad (3)$$

406 This expression can be interpreted as the heat flux convergence that results from

407 the interaction of ENSO in the unperturbed climate (primed quantities) and the changes

408 in the mean climate in response to 2xCO2 (deltas of bar quantities). According to (3) this

409 anomalous heat convergence is due to 1) changes in climatological upwelling $\Delta \overline{w}$,

410 changes in climatological zonal temperature gradient $\Delta \partial \overline{T}/\partial x$, and changes in

411 climatological stratification $\Delta \partial \overline{T}/\partial z$. Here we focus on the effect of the changes in the

412 mean *ocean* climate on ENSO amplitude; however, ENSO amplitude can change due to

413 other processes, such as wind-SST coupling and atmospheric damping. These changes

414 will also lead to a change in Q'_{ocn} via changes in the ENSO anomalies $\Delta \partial T'/\partial z$, $\Delta u'$, and

415 $\Delta w'$ (second term in equation 2).

416 The changes in ocean heat flux convergence due to the changes in the mean

417 climate, i.e. due to changes in the climatological upwelling, zonal temperature gradient,

418 and stratification, are robust among the seven models that have a realistic thermocline

419 feedback (Figures 12 and 13). The first term in (3), the change ENSO heat convergence

420 due to changes in climatological upwelling, is negative, i.e. acts to reduce Q'_{ocn} and thus

weaker ENSO amplitude (Figure 12a and Figure 13 blue bars). This response results from

weaker climatological upwelling in the 2xCO2 climate (i.e, $\Delta\overline{w} < 0$), driven by the

weakening of the Walker circulation (Vecchi and Soden 2007; DiNezio et al. 2009). The

second term in (3) is positive in the upper thermocline and negative in the lower

thermocline (Figure 12b). The resulting increase in ENSO heat flux convergence in the

surface layer (Figure 13, light blue bars) is not a result of a stronger SST gradient, but of

a stronger subsurface zonal temperature gradient (Figure 15a). Note that this zonal

temperature gradient occurs because the time-mean thermocline shoals in the 2xCO2

climate also explaining the anomalous cooling below the thermocline (Figure 12b). The

third term in (3), is positive, i.e. an increase in Q'_{ocn}, due to sharper thermocline in the

2xCO2 climate (Figure 12c). However, note that this response is restricted to the eastern

boundary where anomalous downwelling occurs during the growth of ENSO events

(Figure 3c).

The models do not agree in the combined effect of each of these three processes

$\Delta Q'_{mean}$, despite agreeing on the sign of each individual process. However, $\Delta Q'_{mean}$ is

directly related to the changes in Q'_{tc} ($r = 0.84$, Figure 14), which is the main contributor

to $\Delta Q'_{ocn}$. This relationship is evident in models with large changes in ENSO amplitude,

such as CCSM3.0, FGOALS-g1.0, and GFDL-CM2.1. The reduction in ENSO amplitude

in response to 2xCO2 simulated by CCSM3.0 and FGOALS-g1.0 occurs because the

effect of weaker mean equatorial upwelling dominates. All models simulate reduced

ENSO heat flux convergence due to weaker mean equatorial upwelling (Figure 13, dark

blue bars), however it only leads to weaker ENSO in those models (CCSM3.0, FGOALS-

g1.0, IPSL-CM4) where this term dominates. This effect is less pronounced in GFDL-

444 CM2.1, thus allowing ENSO to strengthen via the effect of the sharper and shallower

445 thermocline on the zonal advection and upwelling terms (Figure 3, light blue and green

446 bars). Unlike the majority of the models, the downwelling anomalies simulated by

447 GFDL-CM2.1 and GFDL-CM2.0 during ENSO events extend into the central Pacific

448 (not shown). For this reason, ENSO is more sensitive to changes in stratification in this

449 model (Figure 13, green bars).

450   There are two exceptions to this explanation for the diverging ENSO responses

451 simulated by this ensemble of climate models. The changes in Q'_{ocn} simulated by MRI-

452 CGM2.3.2a cannot be explained by $\Delta Q'_{mean}$. However, it is possible the stronger ENSO

453 in the 2xCO2 climate, despite the cooling effect of $\Delta Q'_{mean}$, is driven by the (unrealistic)

454 positive net atmospheric heat flux (not shown). The changes in the mean ocean climate

455 results in stronger ocean heat convergence due to thermocline anomalies in CNRM-CM3

456 (Figure 14a, dot 9), however, this fails to translate into stronger ENSO amplitude in the

457 2xCO2 climate. In this model the changes in Q'_{ocn} and Q'_{tc} are confined to the eastern

458 boundary, where the coupling is ineffective in amplifying the changes.

5. Discussion and Conclusions

460   According to this heat budget analysis of the CMIP3 models, ENSO can either

461 weaken or strengthen via changes in the equatorial Pacific Ocean in response to 2xCO2.

462 The changes in ENSO amplitude in the 2xCO2 climate can be directly attributed to

463 2xCO2 forcing because they are larger than unforced centennial changes estimated from

464 the control climate. Whether ENSO amplitude increases or decreases depends on a subtle

465 balance between the changes in ocean heat convergence due to thermocline anomalies vs.

22

zonal currents. The weakening of the Walker circulation and the changes in the thermocline in response to 2xCO2 play opposing roles in this balance. In the 2xCO2 climate, the ocean heat convergence due to thermocline anomalies decreases as the equatorial climatological upwelling weakens in response to the weakening of the Walker circulation/trade winds. In contrast, the heat convergence due to anomalous zonal currents increases as the subsurface zonal temperature gradient strengthens due to a sharper thermocline.

Previous studies also reported diverging ENSO responses, but they attributed it to different mechanisms (Philip and van Oldenborgh 2006, Kim and Jin 2010). Their results show a stronger sensitivity to the changes in stratification and in atmospheric damping, which act to increase and decrease ENSO variability, respectively. In contrast, we find that the inter-model differences in ENSO amplitude are mainly the result of a diverging balance between a weaker thermocline feedback and a stronger zonal advection and upwelling feedback. These studies fitted the model variables into a simplified SST equation (Philip and van Oldenborgh 2006) or to the recharge oscillator (Kim and Jin 2010). Our heat budget decomposes the changes in the temperature equation directly from the models output, thus preserving the spatial correlation between the changes in the mean climate and the ENSO anomalies. This approach also allows us to quantify the different ENSO mechanisms without making any a priori assumptions about their role in ENSO variability.

The BJ index used by Kim and Jin (2010), is very well suited to estimate the strength of the feedbacks, but fails to preserve the spatial patterns of the ENSO anomalies, which are shown here to be important in the interaction between ENSO and

489   the background climate change. For instance, their methodology averages the model

490   variables over the Nino-3 region, thus the spatial correlation between background climate

491   and ENSO anomalies maybe lost. This could be problematic for the upwelling feedback,

492   which is confined to the eastern boundary in the climate models. Thus, averaging over the

493   entire eastern Pacific may render their methodology sensitive to the basin-wide changes

494   in stratification. Moreover, these studies find an important role for atmospheric damping,

495   weakening ENSO. However, unlike observations, atmospheric fluxes play a smaller role

496   in ENSO variability simulated by the models in the pre-industrial climate (Wittenberg et

497   al. 2006). This model bias may render the models insensitive to the changes in

498   atmospheric damping, which should lead to weaker ENSO.

499   A myriad mechanisms can give rise to ENSO variability in models. It is not clear

500   that real world ENSO is governed by these same mechanisms. It is possible that due to

501   the "cold tongue" bias that makes zonal advection stronger, models are not sensitive

502   enough to changes in stratification that can only influence ENSO in eastern Pacific. Thus,

503   the real-world ENSO could be more sensitive to a sharpening of the equatorial

504   thermocline and stronger ENSO events become stronger in response to global warming.

505   It is well known that coupled climate models underestimate the role of atmospheric

506   damping (e.g. Wittenberg et al. 2006; Lloyd et al. 2010). For instance, in the majority of

507   the models the transition from warm to cold events is driven by the ocean heat flux

508   convergence with a very small contribution from atmospheric fluxes (see the composite

509   ENSO heat budget for CCSM3.0; Figure A2b green lines).

510   We have not considered whether changes in high frequency variability, such as

511   the MJO and WWBs, or nonlinearities can result in ENSO changes. Observations suggest

24

512 that random weather noise helps sustain, an otherwise damped ENSO mode (e.g.,

513 Penland and Sardeshmukh, 1995; McPhaden and Yu 1999; Thompson and Battisti 2000,

514 2001; Kessler 2001). We have not considered the nonlinear terms in the heat budget,

515 which can act as a positive or negative feedback to ENSO (Münnich et al. 1991; Jin et al.

516 2003; An 2008, 2009; An and Jin 2004). The sensitivity of these processes to global

517 warming and whether changes in their statistics could lead to changes in ENSO

518 amplitude has not been studied in detail.

519   The heat budget analysis indicates that the 2xCO2 changes in the mean ocean

520 climate play an important role in the changes in ENSO amplitude. The ocean dynamical

521 response to the weakening of the Walker circulation and the increased thermal

522 stratification associated with the surface intensified ocean warming play opposing roles

523 in the ENSO response. The weakening of the mean equatorial upwelling in response to

524 weaker Walker circulation/trade winds drives a reduction in ocean heat convergence due

525 to thermocline anomalies. A stronger mean zonal (subsurface) temperature gradient

526 associated with the increased stratification drives increased ocean heat convergence due

527 to zonal current anomalies.

528   A very tight relationship has been found between inter-model differences in the

529 ENSO response to 2xCO2 and the shape of the zonal wind anomalies in the *control*

530 climate (Merryfield 2006). Models with meridionally narrow zonal wind anomalies tend

531 to exhibit weaker ENSO in response to 2xCO2. Conversely, ENSO strengthens in those

532 models with wider wind anomalies closer to the observed patterns. Models with narrower

533 winds have stronger WSC anomalies, thus the thermocline anomalies in the subsequent

534 phase of the cycle (i.e. the recharge) are stronger. In these models the thermocline

535   feedback dominates over the advection feedback. This is why these models could be

536   more sensitive to 2xCO2 changes in climatological upwelling. The models with wider

537   wind anomalies have relatively weaker WSC anomalies and thermocline deepening

538   during the recharge phase, thus ENSO is less sensitive to the weaker climatological

539   upwelling. This is the same idea put forth by Neale et al. (2008) to explain why CCSM3

540   goes from an oscillator to a series of events when the convection scheme is changed and

541   the wind anomalies become wider.

542   The roles played by the weakening of the Walker circulation and the sharper

543   thermocline presented here can be easily understood by contrast with the effect of these

544   mechanisms on the response of the mean climate. In the mean response, the weaker

545   Walker circulation drives a warming tendency opposed by a cooling tendency due to a

546   sharper thermocline (DiNezio et al. 2009). Since ENSO is a perturbation of the mean

547   climate, opposite roles should be expected from these mechanisms. This is what

548   effectively occurs, with weaker ENSO driven by a weaker Walker circulation and

549   stronger ENSO due to a sharper and shallower thermocline. Note that the sharper

550   thermocline plays a less central role in the ENSO response because its effect is restricted

551   to the eastern boundary where the w' is largest. An exception to this is GFDL-CM2.1,

552   which simulates ENSO with downwelling anomalies in the central Pacific, thus is more

553   sensitive to changes in stratification.

554   The ENSO heat budget presented here has advantages compared with

555   methodologies used by previous studies. Our methodology allows us to compute the

556   contribution of the different ocean processes to heat budget directly from the models

557   output, without making assumptions on the origin of ENSO variability. Moreover, we

558 consider the spatial patterns of the ENSO anomalies and the changes in mean climate

559 when we compute their effect on the heat budget. This feature of our methodology

560 becomes very useful to explore the impact of well-known model biases, which are very

561 likely to influence the sensitivity of the simulated ENSO to global warming.

562   The thermocline feedback, which according to our results is expected to weaken,

563 is still the basis of how El Niño events grow, regardless of whether ENSO is self-

564 sustained or noise-driven. However, changes in the statistics of the stochastic forcing and

565 the details of the interaction between high and low frequency modes needs to be

566 considered in order to fully characterize the sensitivity of ENSO to increasing $CO2$.

567 Moreover, the CMIP3 climate models simulate too weak atmospheric damping of ENSO

568 anomalies compared with observations. Therefore, the real world ENSO could also

569 weaken due to enhanced atmospheric damping in a warmer climate.

570   Despite the very large uncertainty associated with the model projections of ENSO

571 changes, it is clear that the sensitivity of ENSO depends on the balance of weaker

572 upwelling driven by the weakening of the Walker circulation and by the changes in

573 thermocline depth and sharpness. These two responses have different sensitivities to

574 global warming, because the weakening of the Walker circulation is governed by the

575 response of the hydrological cycle. In contrast, the increase in stratification depends on

576 how the surface warming is diffused into the deep ocean. These results indicate that both

577 ENSO simulation and the sensitivity and patterns of tropical climate change need to be

578 improved in order to have reliable projections of ENSO amplitude for the 21st Century.

579 **Acknowledgments**

590

Appendix

a) ENSO Heat Budget

In order to reveal the ocean processes that influence the amplitude of ENSO events and its sensitivity to GW we focus on the growing phase of the ENSO events. We use the tendency of the N3 index, our $\partial N3/\partial t$ index, to study the growth of events. The N3 index is computed for each individual model using SST anomalies (SSTAs) computed with respect to a climatological seasonal cycle averaged over a box in the equatorial cold tongue. This box spans the east-central equatorial Pacific between 5ºN-5ºS, 180º-90ºW and is shifted westward with respect to the conventional Nino-3 region to account for the biases in the coupled models. This same N3 region is used for all models. Before computing the time derivative, the N3 indices are band pass filtered with cut-off frequencies between 18 months and 8 years in order to capture interannual variability.

Consider the heat budget for a surface ocean layer with constant depth H,

$$\rho_0 c_p H \frac{\partial T}{\partial t} = Q_{net} + Q_{ocn}, \qquad (A.1)$$

where $\rho_0 c_p$ = 4.1 10^6 J m^{-3} K^{-1} is the ocean density times the specific heat of sea water, $\partial T/\partial t$ is the tendency of the vertically averaged temperature, Q_{net} is the net atmospheric heat flux, and Q_{ocn} is the convergence of ocean heat transport. Averaging the heat budget (A.1) over the so-called Nino-3 region, and computing anomalies by removing the mean seasonal cycle, we obtain the tendency of the N3 index on the left hand side. For this reason, in this study we linearly regress the different variables

29

610   involved in the heat budget on the normalized $\partial N3/\partial t$ index in order to diagnose the

611   ocean and atmospheric processes involved in the growth of ENSO events.

612   The $\partial N3/\partial t$ index peaks during the development of warm ENSO events (El Nino),

613   during the transition into cold events (LaNina), and during the decay of cold events. The

614   regression of anomalies on the normalized $\partial N3/\partial t$ index contains information of these

615   three instances during the life-cycle of ENSO. Thus the regressions assume that the

616   spatial patterns of warm and cold ENSO events are symmetric. Moreover, the asymmetry

617   between warm and cold events results from nonlinear terms in the temperature equation,

618   therefore our methodology only estimates the heating due to linear terms. In other words,

619   this methodology assumes that warm and cold ENSO events result from the same

620   physical processes. Observations exhibit warm events with larger amplitude and

621   propagation characteristics than cold events, thus rendering this assumption inadequate;

622   however it is reasonable for the simulated ENSO events in most of the CMIP3 models

623   due to the lack of skewness between warm and cold events (van Oldenborgh et al. 2005).

624   The multi-model regression of the heat storage rate, $Q_t = \rho_0 c_p H \partial T/\partial t$, on $\partial N3/\partial t$

625   (Figure 1b) shows a spatial pattern in close agreement with the spatial pattern of the

626   multi-model regression of *SSTA* on the N3 index (Figure A1a). This result illustrates how

627   the developed *SSTA* pattern (Figure A1a) results from the time integration of the heat

628   storage rate (Figure A1b). The depth of integration *H*, used to compute the anomalous

629   heat storage rate Q'_t, is 100 m. The next section discusses why this value is adequate to

630   capture the subsurface changes influencing SSTA during ENSO events. The heat budget

631   (A.1) indicates that anomalies in heat storage rate, Q'_t, could either result from anomalies

632   net atmospheric heat fluxes, Q'_{net}, or anomalous convergence of heat due ocean currents,

633 Q'_{ocn}. The later can be computed as a residual between Q'_t and Q'_{net} using (A.1). The

634 multi-model regressions of Q'_{ocn} and Q'_t on the $\partial N3/\partial t$ index (Figure A1c) shows close

635 agreement in spatial pattern (spatial correlation = 0.99) and magnitude (Figure A1b). This

636 result is not unexpected, but confirms that the heat storage rate associated with growing

637 ENSO events, and hence the amplitude of the developed events, is entirely due to ocean

638 processes. In other words, in the models, as in the actual tropical Pacific, atmospheric

639 fluxes do not play a role during the growth of ENSO events.

640   The dominant role of ocean dynamical processes during an ENSO cycle is clearly

641 seen in the evolution of composites of $SSTA$, Q'_{net}, and Q'_{ocn} averaged over the Nino-3

642 region (Figure A2). All models simulate negligible Q'_{net} when the tendency of $SSTA$ is

643 largest, thus Q'_{ocn} explains the growth of $SSTA$ entirely. For this reason, Q'_{ocn} leads SST

644 by a quarter of a cycle. Moreover inter-model differences in the magnitude of Q'_{ocn}

645 averaged over the N3 region and scaled by the average duration of the growing phase are

646 consistent with the respective ENSO amplitude as measured by the standard deviation of

647 the dimensional N3 index (Figure A3a). However, Q'_{ocn} cannot be readily used to

648 attribute changes in ENSO because is computed as a residual from (A.1).

649   The ocean heat convergence computed using resolved monthly-mean ocean

650 currents Q_{adv}, approximates Q_{ocn} very well (Figure A2, compare solid and dashed black

651 lines). We compute Q_{adv} using monthly mean fields of temperature T, horizontal currents

652 (u,v), and upwelling w following to the methodology of DiNezio et al. (2009):

653 $$Q_{adv} = -\rho_0 c_p \int_{-H}^{0} \left(u \frac{\partial T}{\partial x} + v \frac{\partial T}{\partial y} + w \frac{\partial T}{\partial z} \right) dz . \quad \text{(A.2)}$$

654   The spatial pattern of the ocean heat convergence during the development of ENSO

655   events computed using A.2 (Figure A1b) is strikingly similar to the estimate computed as

656   a residual from A1 (Figure A1d). Note that Q'_{adv} also captures the magnitude and phasing

657   of Q'_{ocn} throughout the ENSO cycle in all models (Figure A2).

658   The advective ENSO heat flux convergence Q'_{adv}, estimated using A.2 captures

659   the inter-model differences averaged over the Nino-3 region (Figure 3Ab). Moreover, the

660   spatial correlation between the multi-model Q'_{adv} and Q'_{ocn} is 0.98 with models ranging

661   from 0.92 (CNRM-CM3) to 0.99 (CCCma-CGCM3.1). Three models (MIROC3.2,

662   CCCma-CGCM3.1, and INM CM3) simulate Q'_{ocn} averaged over the Nino-3 region of

663   less than 20 Wm^{-2}, compared with the remaining models where it is larger than 30 Wm^{-2}.

664   Moreover, as we show in Section 4, this is due to a much weaker thermocline feedback,

665   possibly because the zonal structure of the mean thermocline prevents the interannual

666   anomalies from propagating to the east, where the thermocline is shallow and coupling

667   with SST and winds is more effective. The choice of the depth of integration H, and the

668   limitations of using a constant depth layer are discussed next.

669   **Sensitivity of the Heat Budget to the Depth of Integration**

670   Estimating the ocean heat flux divergence on a constant depth layer (A.2), while

671   being physically consistent, poses limitations to fully describe the influence of some of

672   the ocean processes in heat budget of the ocean mixed layer. Using a constant depth layer

673   could fail to capture the changes involving the thermocline because of its east-west tilt.

674   For instance, the anomalous stratification associated with the deepening of the

675 thermocline prior to warm ENSO events, does not occur on a constant depth surface, and

676 follows the east-west tilt of the climatological thermocline instead (Figure 3b).

677   The depth-dependence of these processes can also be analyzed by computing the

678 temperature tendency and advection terms in each three dimensional grid point. An

679 equatorial section of the temperature tendency (Figure A4.b) and the advection of

680 temperature by zonal and vertical velocity (Figure A4.c) regressed on the $\partial N3/\partial t$ index

681 shows anomalous convergence of heat uniformly distributed in the upper 100 m in the

682 central and eastern Pacific. For this reason we use $H = 100$ to vertically integrate the heat

683 storage rate in (A.1) and the ocean heat divergence due to resolved currents (A.2).

Table of Figures

39

818

Tables

Table 1 – Models with atmosphere and ocean data from 2xCO2 simulations coordinated

by the CMIP3 project.10

References

823

824 An, S.-I., Z. Ye, and W. W. Hsieh, 2006:Changes in the leading ENSO modes associated

825   with the late 1970s climate shift: Role of surface zonal current. *Geophys. Res.*

826   *Lett.*, **33**, L14609.

827 Collins, M., 2000a: Uncertainties in the response of ENSO to Greenhouse Warming.

828   *Geophys. Res. Lett.*, **27**, 3509–3513.

829 Collins, M., 2000b: The El-Niño Southern Oscillation in the second Hadley Centre

830   coupled model and its response to greenhouse warming, *J. Climate*, **13**, 1299–

831   1312.

832 Deser, C., A. Capotondi, R. Saravanan, and A. S. Phillips, 2006: Tropical Pacific and

833   Atlantic climate variability in CCSM3. *J. Climate*, **19**, 2451-2481.

834 DiNezio, P, A. Clement, G. Vecchi, B. Soden, B. Kirtman, and S.-K. Lee: Climate

835   response of the equatorial Pacific to global warming. *J. Climate*, **22**, 4873-4892.

836 Di Nezio, P. N., A. C. Clement, and G. A. Vecchi 2010:Reconciling Differing Views of

837   Tropical Pacific Climate Change. *Eos, Trans. AGU*, *91*(16), 141-142.

838 Fedorov, A. V., and S. G. Philander, 2001: A Stability Analysis of Tropical Ocean–

839   Atmosphere Interactions: Bridging Measurements and Theory for El Niño. *J.*

840   *Climate*, **14**, 3086–3101.

841 Flato, G. M., and G. J. Boer, 2001: Warming asymmetry in climate change simulations.

842   *Geophys. Res. Lett.*, **28**, 195–198.

843 Guilderson T. P.,and D. P. Schrag, 1998: Abrupt shift in subsurface temperatures in the

844   tropical pacific associated with changes in El Niño. *Science*, **281**, 240–243.

845 Guilyardi, E., 2006: El Niño-mean state-seasonal cycle interactions in a multi-model

846   ensemble. *Clim. Dyn.*, **26**, 329–348.

847 Guilyardi E., A. Wittenberg, A. Fedorov, M. Collins, C. Wang, A. Capotondi, G.J. van

848   Oldenborgh, T. Stockdale, 2009: Understanding El Niño in Ocean-Atmosphere

849   General Circulation Models: progress and challenges. *Bull. Amer. Met. Soc.*,

850   published online, in press.

851 Grove, R. 1988: Global Impact of the 1789-93 El Niño. *Nature*, **393**, 318–319.

852 Jin, F.-F. and D. S. Neelin, 1993: Modes of interannual tropical ocean–atmosphere

853   interaction—A unified view. Part I: Numerical Results. *J. Atmos. Sci*, **50**, 3477-

854   3503.

855 Kirtman, B. P., D. M. Straus, D. Min, E. K. Schneider, and L. Siqueira, 2009: Toward

856   linking weather and climate in the interactive ensemble NCAR climate model.

857   *Geophys. Res. Lett.*, **36**, L13705, doi:10.1029/2009GL038389.

858 Kirtman, B. P., K. Pegion, and S. Kinter, 2005: Internal atmospheric dynamics and

859   climate variability. J. Atmos. Sci., 62, 2220-2233.Knutson, T. R. and S. Manabe,

860   1995: Time-mean response over the tropical Pacific to increased CO_2 in a

861   coupled ocean-atmosphere model. *J. Climate*, **8**, 2181–2199.

862 Knutson, T. R., S. Manabe, S., and D. Gu, 1997: Simulated ENSO in a global coupled

863   ocean-atmosphere model: Multidecadal amplitude modulation and CO2

864   sensitivity. *J. Climate*, **10**, 42–63.

865   Harrison, D. E., and N. K. Larkin, 1997: Darwin sea level pressure, 1876–1996: Evidence

866   for climate change? Geophys. Res. Lett., 24, 1775–1782.

867   Hasumi, H., and S. Emori, Eds., 2004: K-1 coupled GCM(MIROC) description, *K-1*

868   *Tech. Rep.*, *1*, 34 pp.

869   Kessler, W. S., 2003: Is ENSO a cycle or a series of events? *Geophys. Res. Lett.*, **29**,

870   2125, doi:10.1029/2002GL015924

871   Liu, Z., S. J. Vavrus, F. He, N. Wen, and Y. Zhang, 2006: Rethinking tropical ocean

872   response to global warming: The enhanced equatorial warming. *J. Climate*, **18**,

873   4684–4700.

874   Manabe, S. and R. J. Stouffer, 1994: Multiple-century response of a coupled ocean-

875   atmosphere model to an increase of atmospheric carbon dioxide. *J. Climate*, **7**, 5–

876   23.

877   Marti, O. and Coauthors, 2005: The new IPSL climate system model: IPSL-CM4, Note

878   du Pole de Modelisation no 26, Institut Pierre Simon Laplace des Sciences de

879   l'Environnement   Global.

880   http://dods.ipsl.jussieu.fr/omamce/IPSLCM4/DocIPSLCM4/FILES/socIPSLCM4.

881   pdf.

882   Meehl, G. A., G. W. Branstator, and W. M. Washington, 1993: Tropical Pacific

883   Interannual Variability and CO2 Climate Change. *J. Climate*, **6**, 42–63.

884   Meehl, G. A., P. R. Gent, J. M. Arblaster, B. L. Otto-Bliesner, E. C, Brady, and A. Craig,

885   2001: Factors that affect the amplitude of El Niño in global coupled climate

886   models. *Clim. Dyn.*, **17**, 515–526.

887 Meehl, G.A., H. Teng, and G.W. Branstator, 2006: Future changes of El Niño in two
888   global coupled climate models. Clim. Dyn., 26, 549–566.

889 Meehl, G. A., and Coauthors, 2007: Global Climate Projections. Climate Change 2007:
890   The Physical Science Basis. Contribution of Working Group I to the Fourth
891   Assessment Report of the Intergovernmental Panel on Climate Change.
892   Cambridge University Press, 747–845.

893 McPhaden, M. J. and X. Yu, 1999: Equatorial waves and the 1997–98 El Niño. *Geophys.*
894   *Res. Lett.*, **26**, 2961–2964.

895 Merryfield, W., 2006: Changes to ENSO under CO2 doubling in a multimodel ensemble.
896   *J. Climate*, **19**, 4009–4027.

897 Neale, R. B., J. H. Richter, and M. Jochum, 2008: The Impact of Convection on ENSO:
898   From a Delayed Oscillator to a Series of Events. *J. Climate*, **21**, 5904-5924.

899 Neelin, J. D., 1991: The slow sea surface temperature mode and the fast-wave limit:
900   Analytic theory for tropical interannual oscillation and experiments in a hybrid
901   coupled model. *J. Atmos. Sci.,* **48,** 584–606.

902 Neelin, J. D., D. S. Battisti, A. C. Hirst, F.-F. Jin, Y. Wakata, T. Yamagata, and S. E.
903   Zebiak, 1998: ENSO theory. *J. Geophys. Res.*, **103**(C7), 14,261–14,290.

904 Penland, C., and P. D. Sardeshmukh, 1995: The optimal growth of tropical sea surface
905   temperature anomalies. *J. Climate*, **8**, 1999–2024.

906 Rajagopalan, B., U. Lall, and M. A. Cane, 1997: Anomalous ENSO occurrences: An
907   alternative view. *J. Climate*, **10**, 2351–2357.

908 Salas-Mélia, D., F. Chauvin, M. Déqué, H. Douville, J. F. Gueremy, P. Marquet, S.

909   Planton, J. F. Royer, and S. Tyteca, 2005: Description and validation of the

910   CNRM-CM3 global coupled model, CNRM working note 103.

911 Schopf, P. S., and M. J. Suarez, 1988: Vacillations in a coupled ocean–atmosphere

912   model. *J. Atmos. Sci.,* **45,** 549–566.

913 Tett S., 1995: Simulation of El Niño/southern oscillation like variability in a global

914   AOGCM and ifs reponse to CO2 increase. *J. Climate*, **8**, 1473–1502.

915 Thompson, C. J., and D. S. Battisti, 2000: A linear stochastic dynamical model of ENSO.

916   Part I: model development. *J. Climate*, **13**, 2818–32.

917 Thompson, C. J., and D. S. Battisti, 2001: A linear stochastic dynamical model of ENSO.

918   Part II: analysis. *J. Climate*, **14**, 445–66.

919 Timmermann A., Oberhuber J., Bacher A., Esch M., and Latif M., 1999: Increased El

920   Niño frequency in a climate model forced by future greenhouse warming. *Nature*,

921   **398**, 694–696.

922 Trenberth, K. E., and T. J. Hoar, 1997: El Niño and climate change. *Geophys. Res. Lett.*,

923   **24**, 3057–3060.

924 Urban F. E., J. E. Cole, and J. T. Overpeck, 2000: Influence of mean climate change on

925   climate variability from a 155-year tropical Pacific coral record. *Nature*, **407**,

926   989–993.

927 van Oldenborgh, G. J., S. Y. Philip, and M. Collins, 2005: El Niño in a changing climate:

928   a multi-model study. *Ocean Sci.*, **1**, 81–95.

929   Vecchi, G. A., B. J. Soden, A. T. Wittenberg, I. M. Held, A. Leetmaa, and M. J. Harrison,

930   2006: Weakening of tropical Pacific atmospheric circulation due to anthropogenic

931   forcing. *Nature*, **441**, 73–76.

932   Vecchi, G. A., and B. J. Soden, 2007: Global warming and the weakening of the tropical

933   circulation. *J. Climate*, **20**, 4316–4340.

934   Vecchi, G. A., A. Clement, and B. J. Soden, 2008. Examining the tropical Pacific's

935   response to global warming. *EOS, Trans. Amer. Geophys. Union,* **89**, 8183.

936   Vecchi, G.A. and A.T. Wittenberg, 2010: El Niño and our future climate: where do we

937   stand? Wiley Interdisciplinary Reviews: Climate Change, pp.1757-778DOI:

938   10.1002/wcc.33

939   Volodin, E. M., and N. A. Diansky, 2004: El Niño reproduction in coupled general

940   circulation model. *Russ. Meteor. Hydrol.*, **12**, 5–14.

941   Wittenberg, A. T., 2009: Are historical records sufficient to constrain ENSO simulations?

942   Geophys. Res. Lett., 36, L12702. doi:10.1029/2009GL038710.

943   Wittenberg, A. T., A. Rosati, N.-C. Lau, and J. J. Ploshay, 2006: GFDL's CM2 global

944   coupled climate models. Part III: Tropical Pacific climate and ENSO. *J. Climate.*,

945   **19**, 698-722.

946   Yeh S.-W. and B. P. Kirtman, 2007: ENSO amplitude changes due to climate change

947   projections in different coupled models. *J. Climate*, **20**, 203–217.

948   Yu, Y. Q., X. H. Zhang, and Y. F. Guo, 2004: Global coupled ocean-atmosphere general

949   circulation models in LASG/IAP. *Adv. Atmos. Sci.*, **21**, 444–455.

950 Yukimoto, S., and A. Noda, 2002: Improvements in the Meteorological Research

951   Institute Global Ocean-Atmosphere Coupled GCM (MRI-CGCM2) and its

952   climate sensitivity. Tech. Rep. 10, NIES, Japan, 8 pp.

953 Zhang Q., Y. Guan, and H. Yang, 2008: ENSO amplitude change in observation and

954   coupled models. *Adv. Atmos. Sci.*, **25**, 361–366.

955

Tables

Model	Reference	Institution, Country	Model Resolution	
			Atmosphere lat. x long .	Ocean lat. x long.
FGOALS-g1.0	Yu et al. 2004	LASG/Institute of Atmospheric Physics, China	T42 L26 (2.8° × 2.8°)	1° × 1° L33
MIROC3.2	Hasumi and Emori 2004	Center for Climate System Research (University of Tokyo), National Institute for Environmental Studies, and Frontier Research Center for Global Change (JAMSTEC), Japan	T42 L20 (2.8° × 9 2.8°)	0.5–1.4° × 1.4° L43
CCSM3.0	Deser et al. 2006	National Center for Atmospheric Research, USA	T42 L26 (2.8° × 2.8°)	1/3°–1° × 1° L40
IPSL-CM4	Marti et al. 2005	Institut Pierre Simon Laplace, France	2.5° × 3.75° L19	1–2° × 2° L31
GFDL-CM2.0 and GFDL-CM2.1	Wittenberg et al. 2006	National Oceanic and Atmospheric Administration Geophysical Fluid Dynamics Laboratory, USA	2° × 2.5° L24	1/3°–1° × 1° L50
INM-CM3.0	Volodin and Diansky 2004	Institute of Numerical Mathematics, Russia	2.5°×2° L33	5°×4° L21

CCCma-CGCM3.1	Flato and Boer 2001	Canadian Centre for Climate Modelling and Analysis, Canada	T47 L31	1.85°×1.85° L29
CNRM-CM3	Salas-Mélia et al. 2005	Meteo-France/Centre National de Recherches Meteorologiques, France	T63 L45	2°×0.5° L31
MRI CGCM2.3.2	Yukimoto and Noda 2002	Meteorological Research Institute, Japan.	T42 L30	2.5°×0.5° L23

957   **Table 1 –** Models with atmosphere and ocean data from 2xCO2 simulations coordinated by the CMIP3 project.

958

959 # Figures
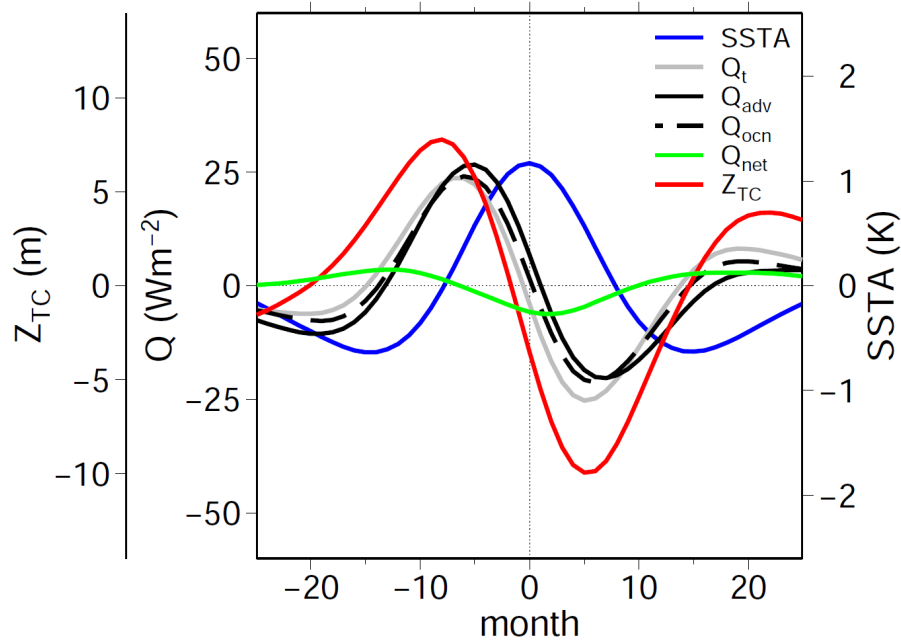
960

961 **Figure 1 –** Multi-model composite heat budget during the development, transition, and decay of
962 warm ENSO events. Month zero is when sea surface temperature anomalies (*SSTA*) peaks.
963 Black solid and dashed lines are the ocean dynamical heating computed using resolved currents
964 (Q'_{adv}) and as a residual of the heat budget (Q'_{ocn}) respectively. The green line is the net
965 atmospheric heat flux (Q'_{net}). Positive values of heating terms indicate a warming tendency. The
966 red line is the depth of the thermocline (Z_{TC}). All variables are seasonal anomalies averaged over
967 the models Nino-3.4 region (180º-110ºW 2.5ºS-2.5ºN).

968
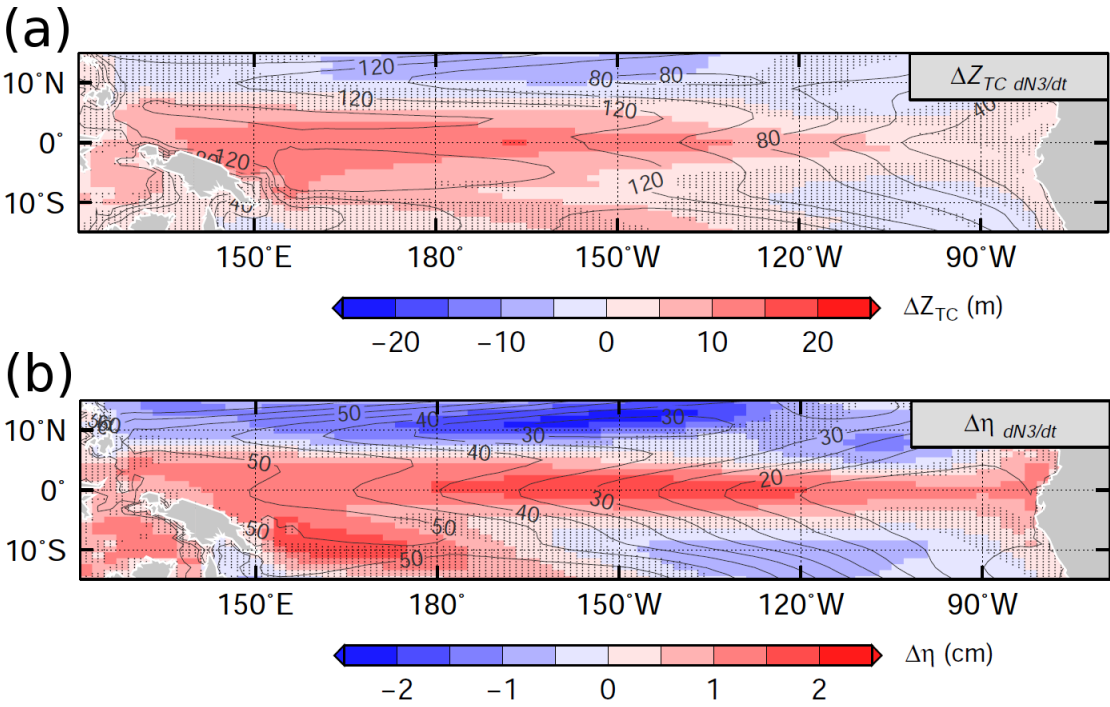
Figure 2 – Multi-model mean regression of (a) thermocline depth and (b) sea level on the normalized ∂N3/∂t index. In this and all subsequent figures stippling shows where the multi-model regressions are *not* robust. A multi-model regression is considered robust when all ten models agree in sign with the multi-model mean. Contours show the multi-model ensemble-mean annual-mean climatology. The contour intervals are 20 m and 2 cm respectively.

976

977
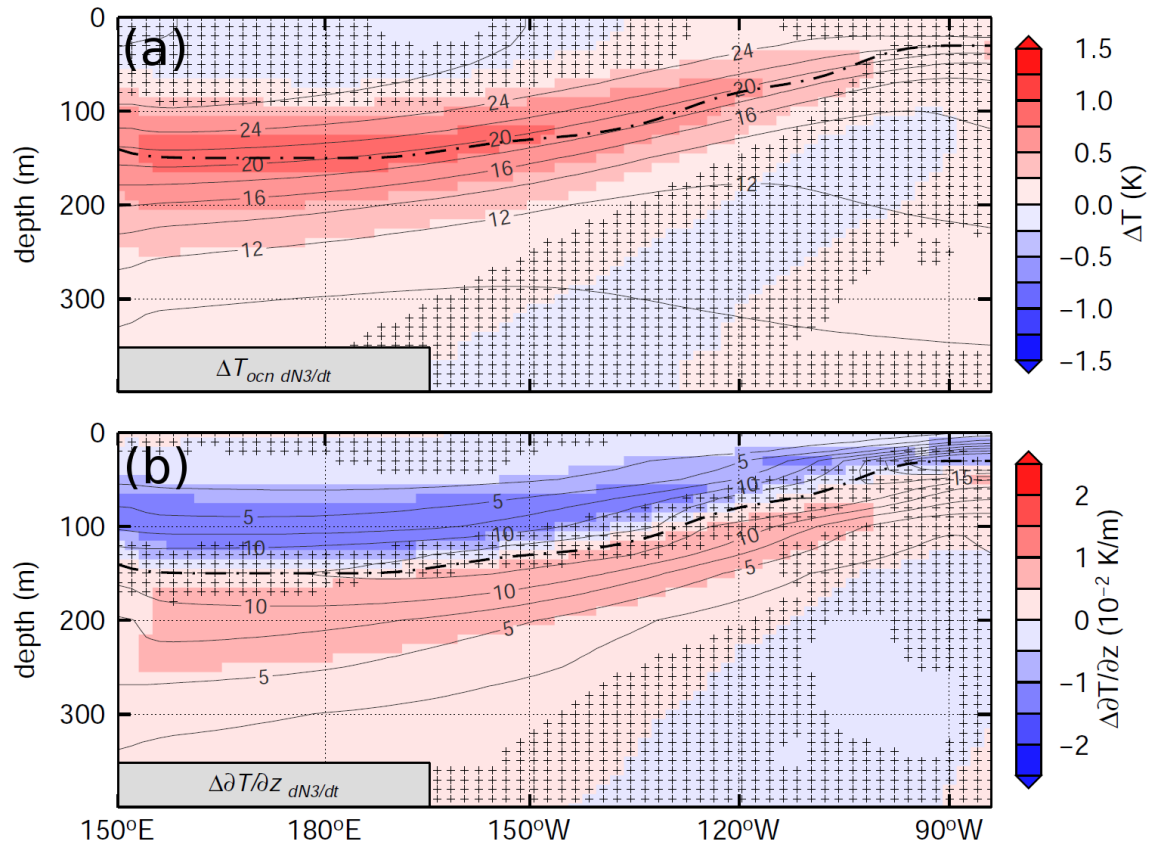
Figure 3 – Multi-model mean regressions of (a) subsurface temperature anomalies and (b) vertical temperature gradient anomalies on the normalized $\partial N3/\partial t$ index. The equatorial sections are averaged over the 2ºS and 2ºN latitude band. Contours show the multi-model ensemble-mean annual-mean climatology of each variable. The dash-dotted lines indicate the depth of the thermocline, i.e. the maximum of $\partial T/\partial z$. The contour intervals are 2°C and 2.5 10^{-2} K m^{-1} respectively.
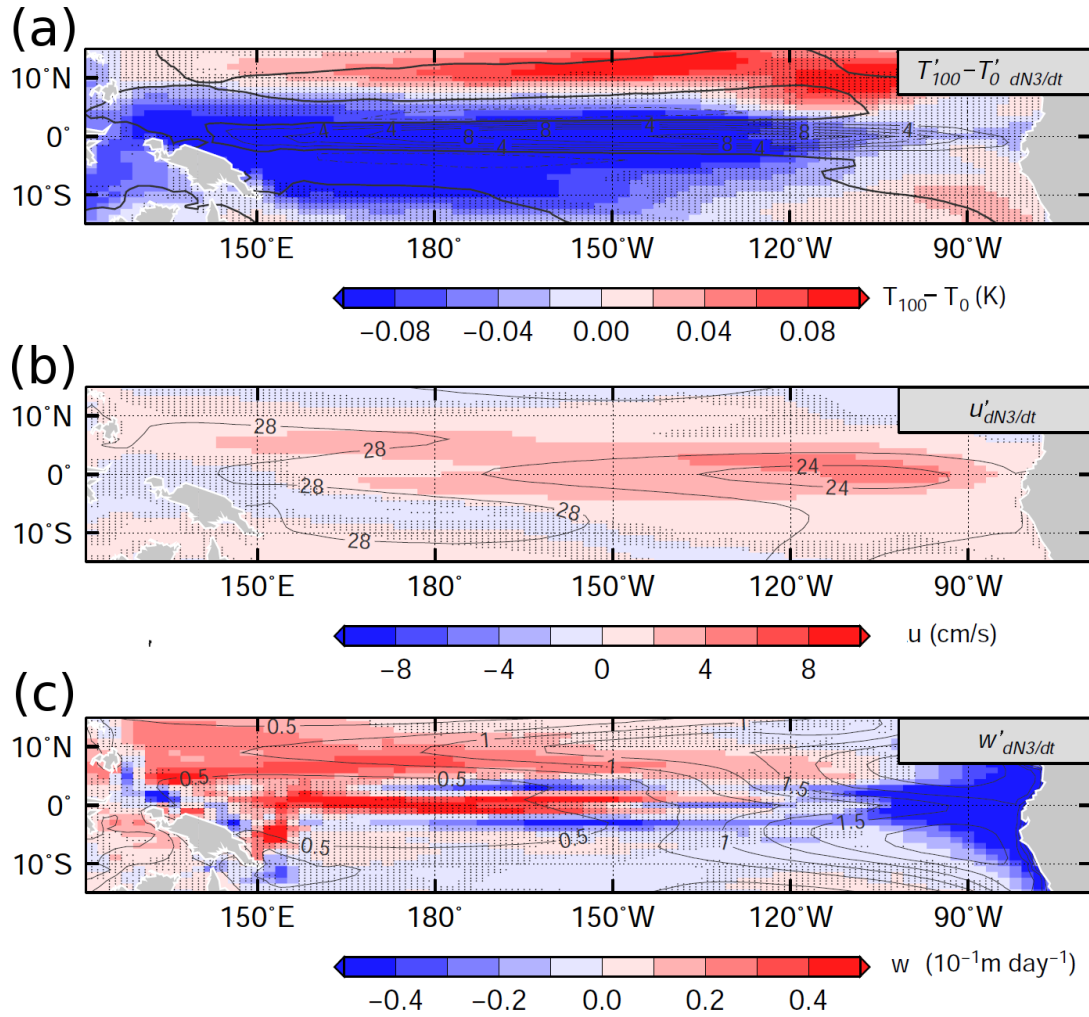
Figure 4 – Multi-model mean regression of (a) vertical stratification, (b) zonal velocity, and (c) upwelling anomalies on the normalized $\partial N3/\partial t$ index. These variables are averaged over the the upper 100 m surface layer before computing the regressions. Contours show the multi-model ensemble-mean annual-mean climatology of (a) upwelling averaged over the surface layer, (b) sea surface temperature, and (c) vertical stratification averaged over the surface layer. The contour interval is $2 \; 10^{-5}$ m s^{-1}, 2°C, and 0.25 K m^{-1} respectively.
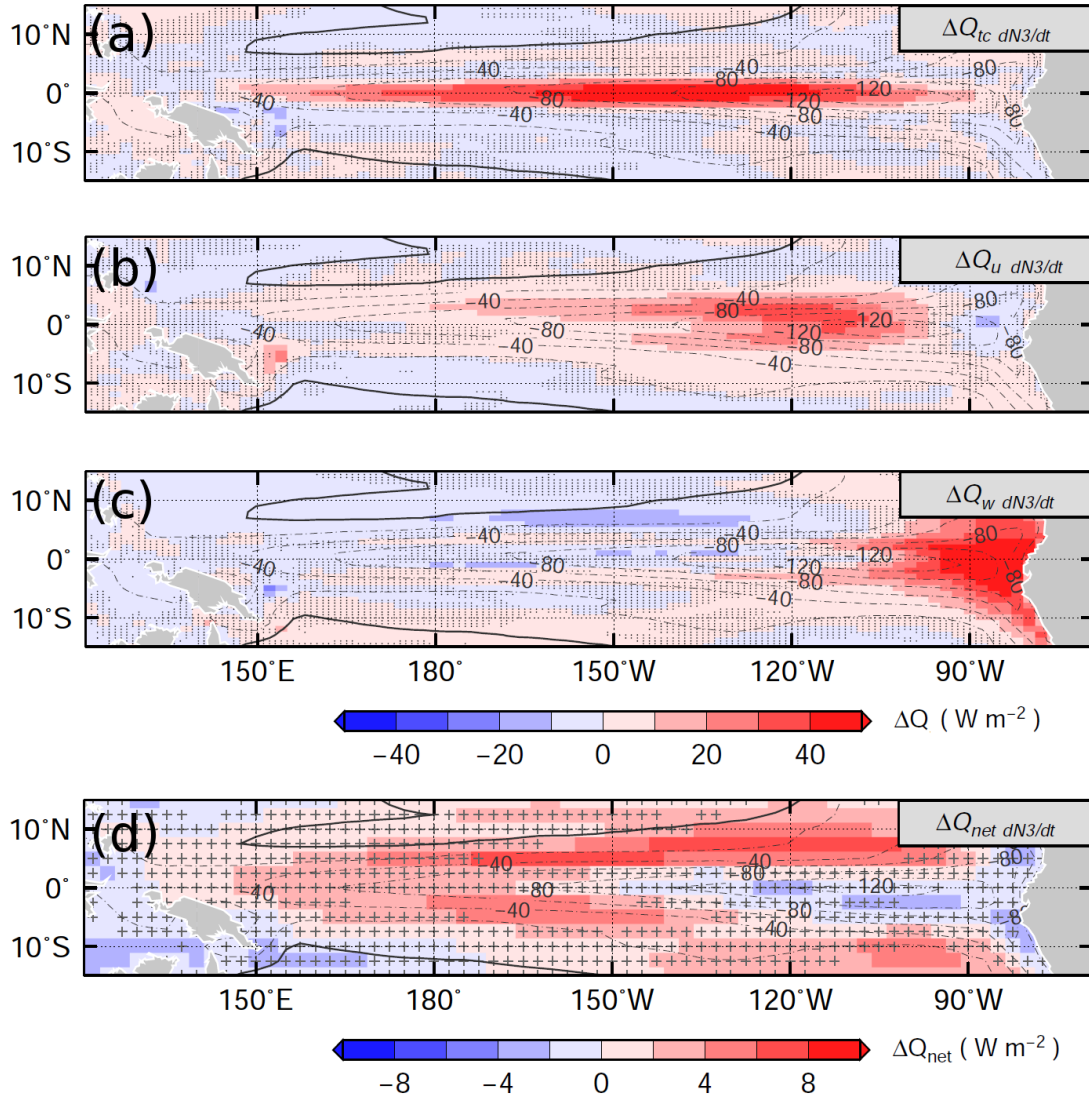
Figure 5 – Multi-model mean regression of the ocean heat convergence due to (a) advection of thermocline anomalies by climatological upwelling, (b) advection of climatological zonal temperature gradient by zonal current anomalies, and (c) advection of climatological vertical temperature gradient by upwelling anomalies on the normalized $\partial N3/\partial t$ index. (d) Multi-model regression of air-sea heat flux anomalies on the normalized $\partial N3/\partial t$ index. Contours show the multi-model ensemble-mean annual-mean ocean heat divergence (cooling). The contour interval is 20 W m^{-2}.

1000
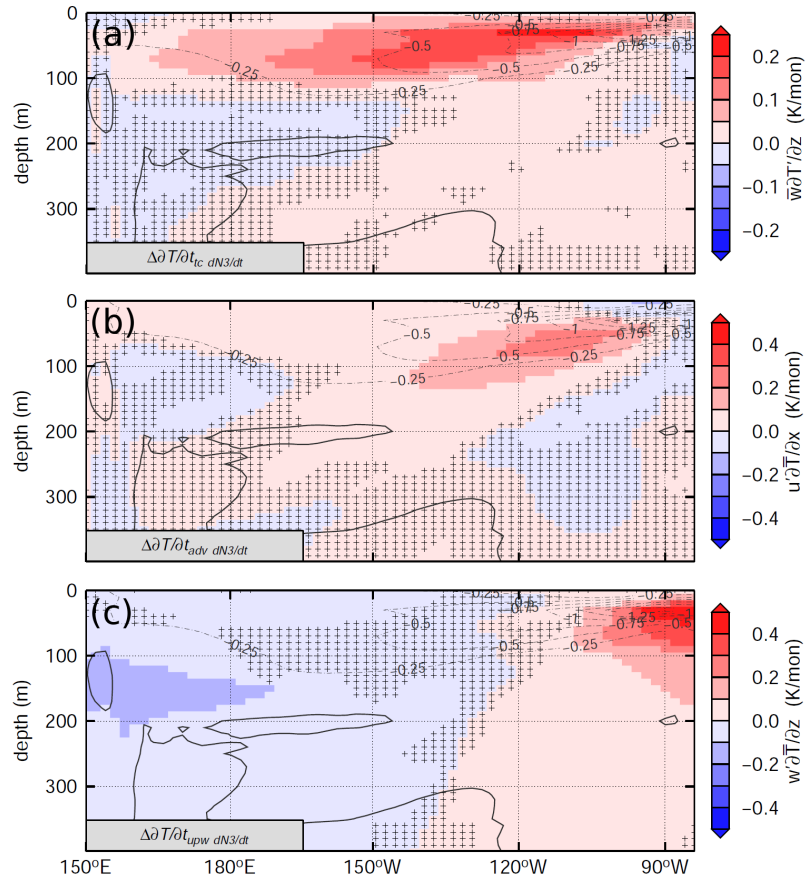
1001

Figure 6 – (a) Multi-model mean regressions on the normalized ∂N3/∂t index of subsurface temperature tendency anomalies due to (a) thermocline anomalies, (b) zonal velocity anomalies, and (c) upwelling anomalies. The equatorial sections are averaged over the 2ºS and 2ºN latitude band. Contours show the multi-model ensemble-mean annual-mean climatology of temperature tendency due to zonal and vertical currents. The contour interval is 0.25 K mon^{-1}.
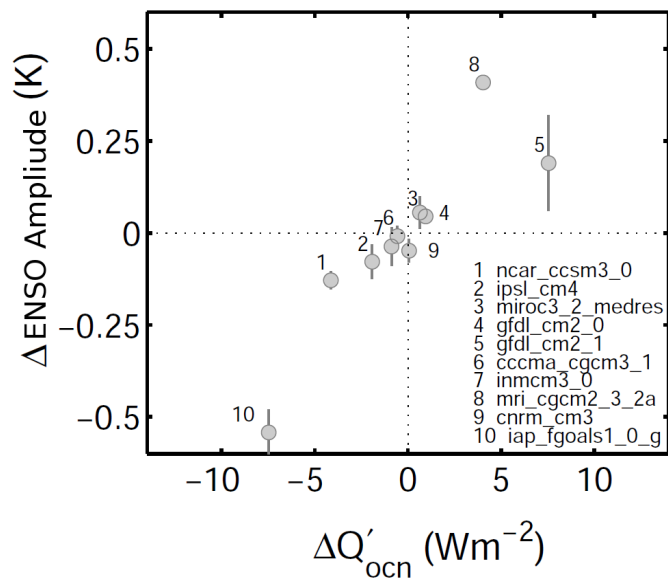
1007
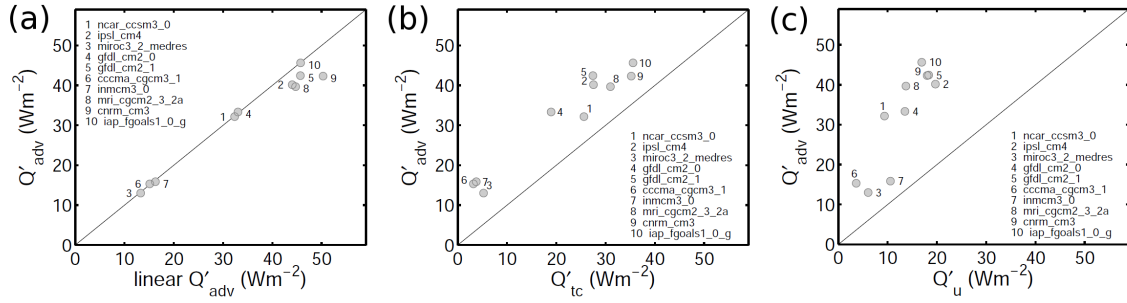
1008

1009 **Figure 7** – Ocean heat convergence during the development of ENSO events computed from

1010 resolved currents (Q'_{adv}) vs. (a) the linear ocean heat convergence, (b) the heat convergence due

1011 to thermocline anomalies, and (c) the heat convergence due to zonal current anomalies. All

1012 variables are averaged over the Nino-3.4 region (180º-110ºW 2.5ºS-2.5ºN).

1015 **Figure 8** – 2xCO2 changes in ENSO amplitude (y-axis) vs. 2xCO2 changes in ocean heat

1016 convergence during the development phase of ENSO events (Q'_{ocn}, x-axis). The error bars

1017 indicate the 1σ interval of unforced changes in ENSO amplitude in the control experiment. The

1018 Q'_{ocn} values are averaged over the Nino-3 region (5ºN-5ºS, 180º-90ºW) before computing the

1019 2xCO2 difference.
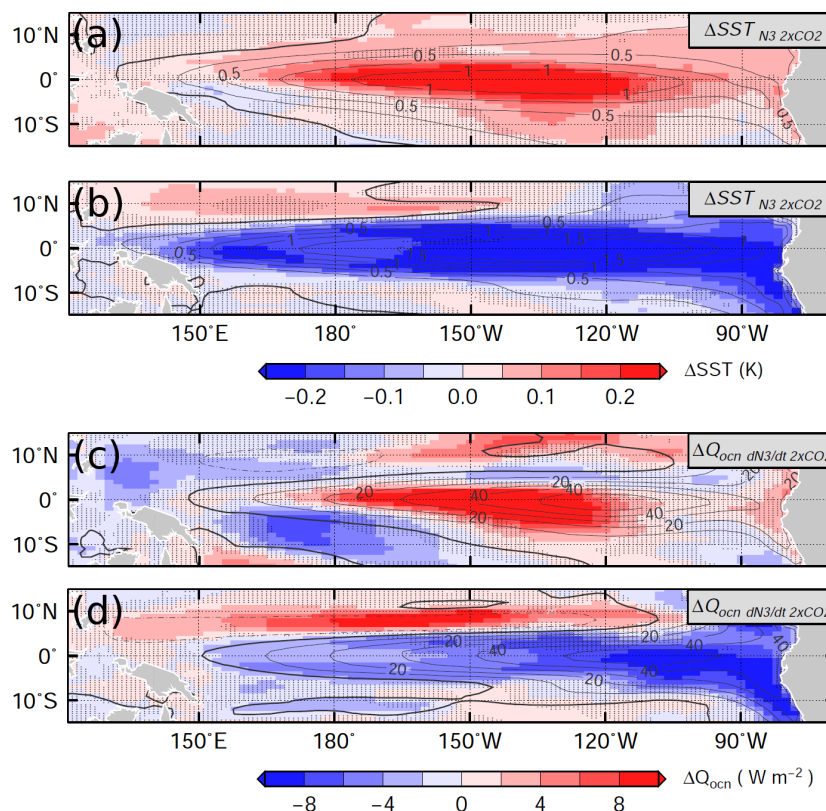
Figure 9 – Change in multi-model mean regressions of sea surface temperature anomalies (*SSTA*) on the normalized N3 index for models with (a) stronger and (b) weaker ENSO in the 2xCO2 climate. Change in multi-model mean regressions of ocean dynamical heating anomalies (Q'_{ocn}) on the normalized ∂N3/∂t index for models with (c) stronger and (d) weaker ENSO in the 2xCO2 climate. The models with stronger ENSO are GFDL-CM2.1, GFDL-CM2.0, and MRI-CGM2.3.2a. The models with weaker ENSO are CCSM3.0, FGOALS-g1.0, and IPSL-CM4. In this figure a multi-model change is considered robust when all three models agree in sign with the multi-model mean. Contours show the multi-model regressions in the control climate. The contour intervals are 0.25°C and 10 Wm^{-2} respectively.

1030
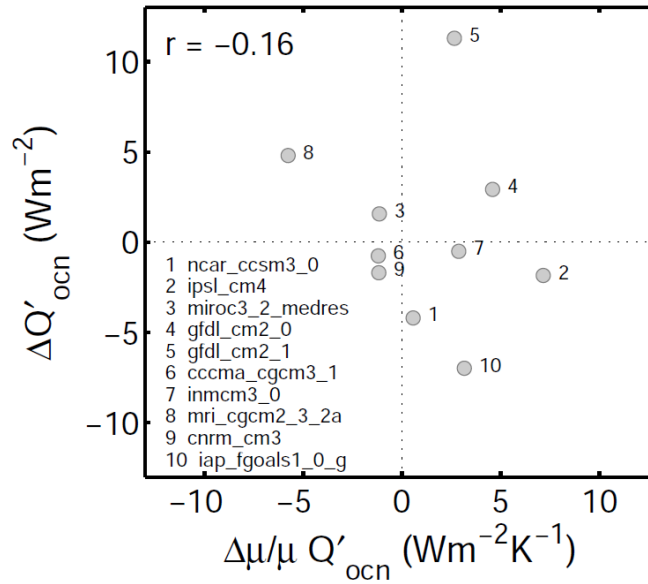
1031

1032 **Figure 10 –** 2xCO2 changes in ocean heat convergence during the development phase of ENSO

1033 events ($\Delta Q'_{ocn}$) (y-axis) vs. fractional change in wind-SST coupling ($\Delta\mu/\mu$) (x-axis) in each

1034 individual model. The fractional changes in wind-SST coupling ($\Delta\mu/\mu$) are scaled by Q'_{ocn} to

1035 facilitate the comparison with the changes $\Delta Q'_{ocn}$. Both $\Delta Q'_{ocn}$ and Q'_{ocn} are averaged over the

1036 Nino-3.4 region (180º-110ºW 2.5ºS-2.5ºN).

Figure 11 – (a) 2xCO2 changes in ENSO heat convergence computed as (a) a residual (Q'_{ocn}) (y-axis) vs. computed from resolved currents (Q'_{adv}) (x-axis) in each individual model. Changes in Q'_{adv} (y-axis) vs. changes in ocean heat convergence due to (a) thermocline anomalies (Q'_{tc}), (c) upwelling anomalies (Q'_{tc}), and (d) zonal current anomalies (Q'_{u}) (x-axis). All changes are averaged over the Nino-3.4 region (180º-110ºW 2.5ºS-2.5ºN).

1044

1045

1046 **Figure 12 –** (a) Multi-model change in subsurface temperature tendency anomalies due to

1047 changes in (a) climatological upwelling and thermocline anomalies, (b) climatological zonal

1048 temperature gradient and zonal velocity anomalies, and (c) stratification and upwelling anomalies.

1049 The equatorial sections are averaged over the 2ºS and 2ºN latitude band. Contours show the

1050 multi-model ensemble-mean temperature tendency during the growth of ENSO events due to (a)

1051 thermocline, (b) zonal current, and (c) upwelling anomalies in the pre-industrial climate. The
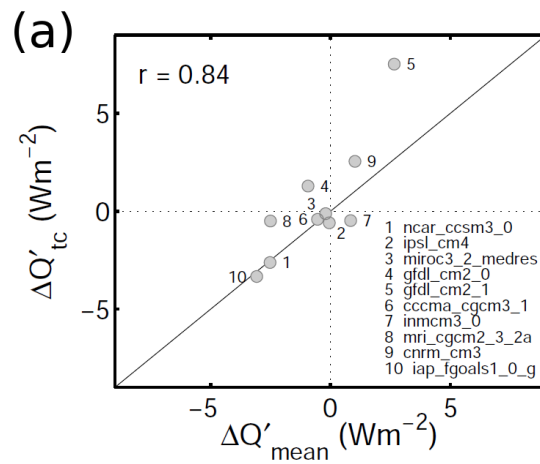
1052 contour interval is 0.1 K mon^{-1}.

1053
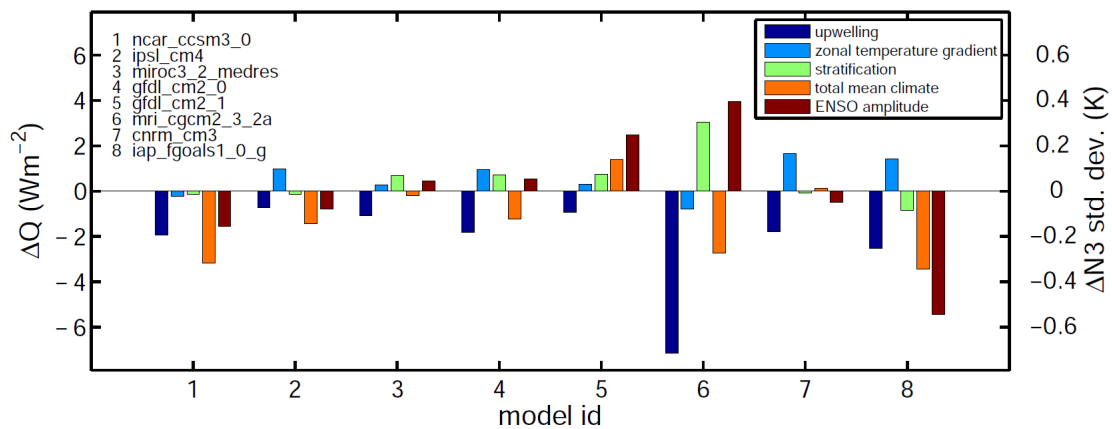
Figure 13 – 2xCO2 changes in ENSO heat convergence due to changes in climatological upwelling (blue), zonal temperature gradient (cyan), stratification (green). Total 2xCO2 changes in ENSO heat convergence due to changes in the mean climate (orange) and changes in ENSO amplitude (brown). All changes are averaged over the Nino-3.4 region (180°-110°W 2.5°S-2.5°N). Only models that simulate 2xCO2 changes in ENSO amplitude larger than the 1σ range of unforced ENSO centennial variability are shown.

1054
1055
1056
1057
1058
1059

1060

(a)

r = 0.84

1 ncar_ccsm3_0
2 ipsl_cm4
3 miroc3_2_medres
4 gfdl_cm2_0
5 gfdl_cm2_1
6 cccma_cgcm3_1
7 inmcm3_0
8 mri_cgcm2_3_2a
9 cnrm_cm3
10 iap_fgoals1_0_g

1062   **Figure 14 –** (a) 2xCO2 changes in ENSO heat convergence due to thermocline anomalies (y-

1063   axis) vs. changes in ENSO heat convergence due to changes in the men climate (x-axis). All

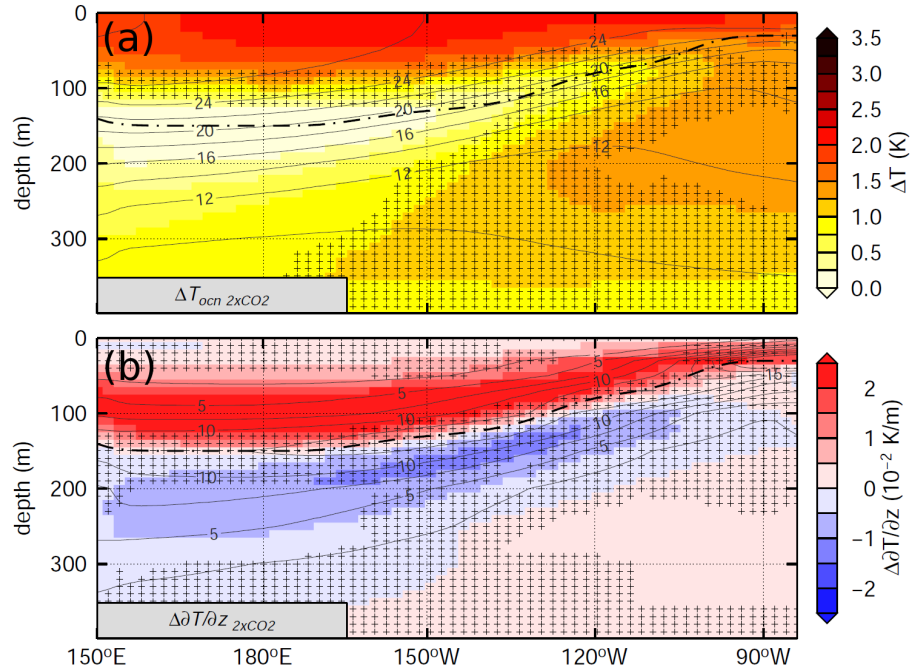1064   changes are averaged over the Nino-3.4 region (180º-110ºW 2.5ºS-2.5ºN).

1065

1066

1067

Figure 15 – Multi-model mean 2xCO2 change in subsurface (a) temperature and (b) vertical temperature gradient on the equatorial Pacific. The dashed dotted line is the depth of the thermocline in the pre-industrial climate. The equatorial sections are averaged over the 2ºS and 2ºN latitude band. Contours show the multi-model ensemble-mean annual-mean climatology. The contour intervals are 2 K and 10^{-2} 5 K m^{-1} respectively.

1073
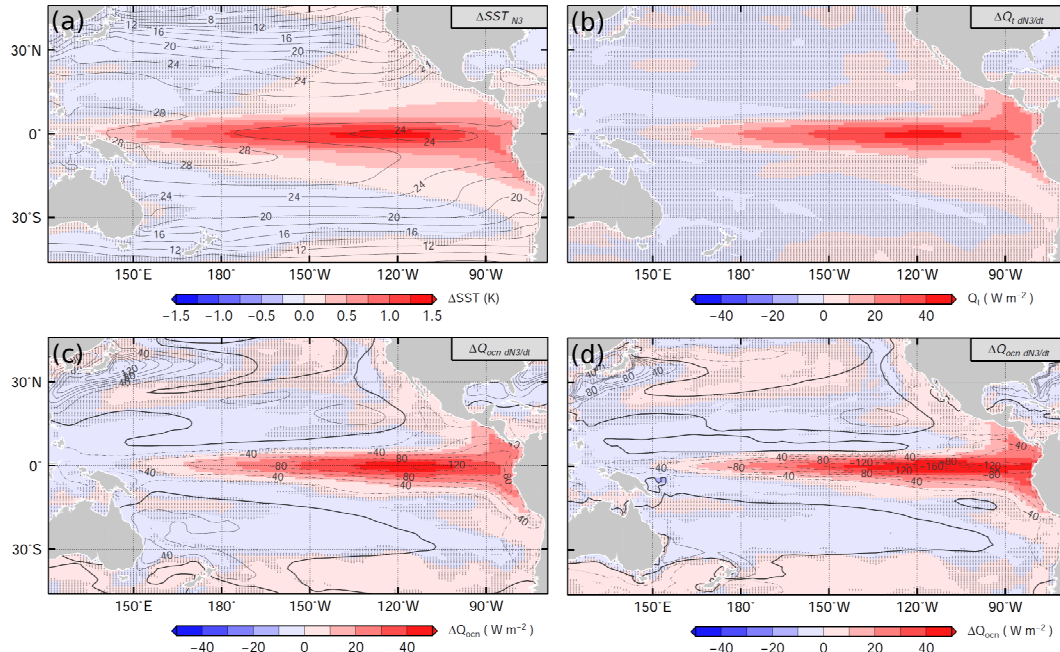
Figure A1 – (a) Multi-model mean regressions of sea surface temperature anomalies on the normalized N3 index. Multi-model mean regression of (b) heat content tendency, (c) ocean dynamical heating, and (c) ocean dynamical heating from resolved monthly fields regressed on the normalized $\partial N3/\partial t$ index. Contours show the multi-model ensemble-mean annual-mean climatology of each variable, with the exception of the climatological heat storage which is zero The contour interval is 2°C and 20 Wm^{-2} respectively.
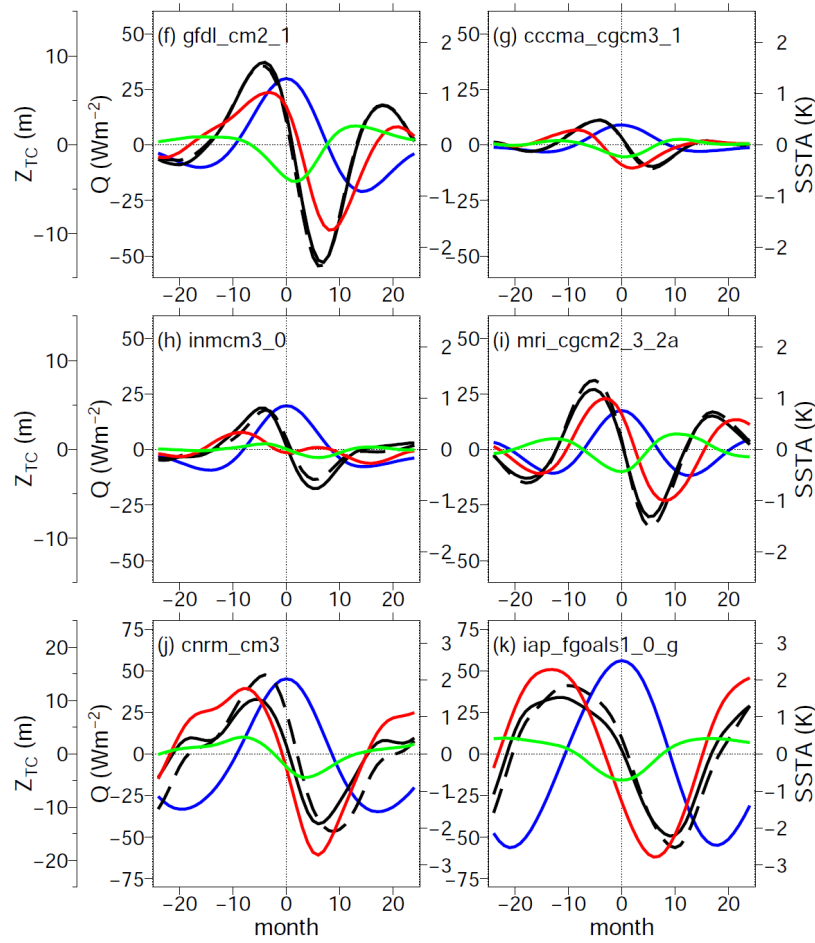
1081

1082

1083
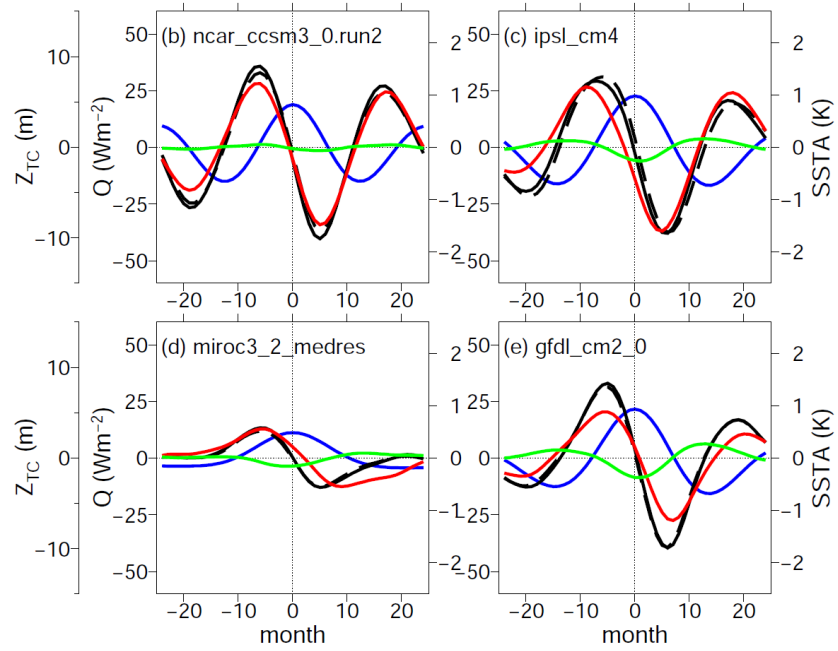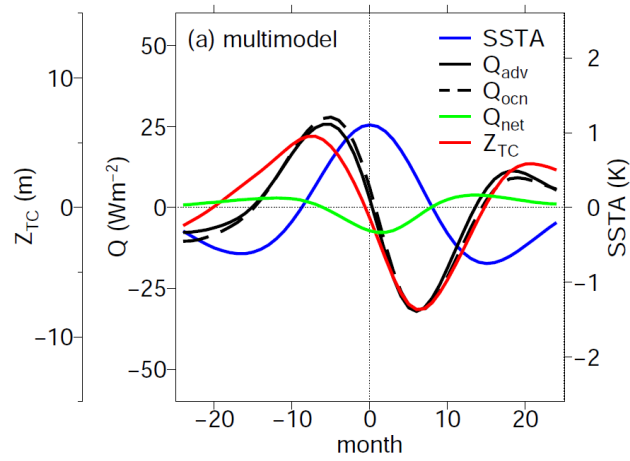
Figure A2 – Heat budget during the evolution of a composite of ENSO events for (a) the multi-model mean and (b to k) each individual model. Month zero is when sea surface temperature anomalies (*SSTA*), i.e. the N3 index, peaks. Black solid and dashed lines are the ocean dynamical heating computed using resolved currents (Q'_{adv}) and as a residual of the heat budget (Q'_{ocn}) respectively. The heat storage budget is computed for the upper 100 m layer of the ocean. and Green lines are the net atmospheric heat flux (Q'_{net}). Positive values of heating terms indicate a warming tendency. Red lines are the depth of the thermocline (Z_{TC}). All variables are seasonal anomalies averaged over the Nino-3 region (5ºN-5ºS, 180º-90ºW). Note that the vertical scales are different for models CNRM-CM3 (j) and FGOALS-g1.0 (k) because ENSO events are stronger in these models.
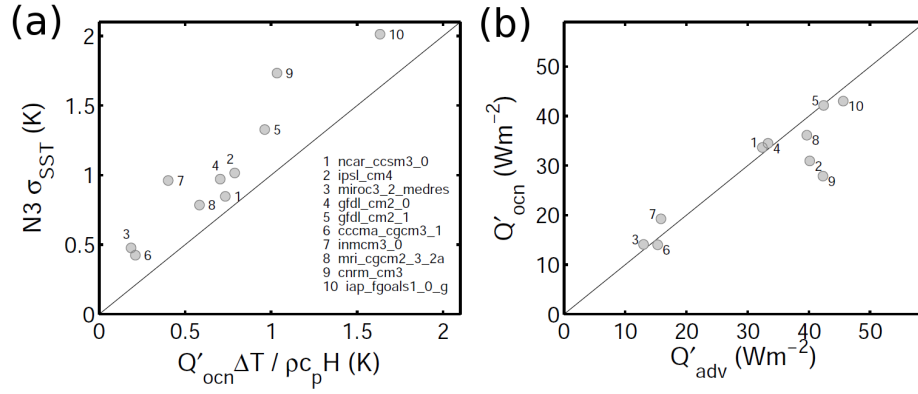
1094

Figure A3 – (a) ENSO amplitude vs. ENSO heat convergence in each model. The ENSO heat convergence is averaged over Nino-3 region. This value is then multiplied by the heat capacity and the duration of the growing phase to approximate the time-integration of the ocean heat convergence that leads to the fully-developed ENSO amplitude. (b) ENSO heat convergence computed as a residual from the heat budget (Q'_{ocn}) vs. ENSO heat convergence computed as the temperature advection by monthly-mean fields (Q'_{adv}) in each individual model.
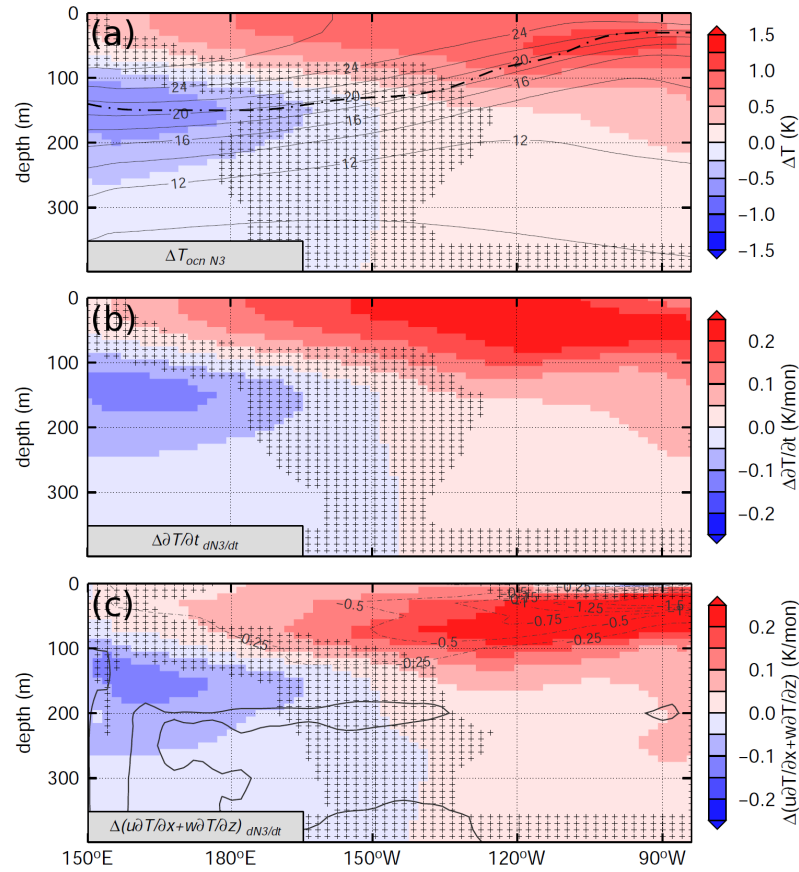
Figure A4 – (a) Multi-model mean regressions of subsurface temperature anomalies on the normalized N3 index. Multi-model mean regression of (b) temperature tendency and (c) temperature advection by zonal and vertical currents regressed on the normalized ∂N3/∂t index. The equatorial sections are averaged over the 2ºS and 2ºN latitude band. Contours show the multi-model ensemble-mean annual-mean climatology of each variable, with the exception of the climatological temperature tendency, which is zero. The dash-dotted lines indicate the depth of the thermocline, i.e. the maximum of ∂T/∂z. The contour interval is 2°C and 0.25 K mon^{-1} respectively.

1114